The Geological Society of America
Special Paper 548

Glacier development in continental climate regions of central Asia

Jigjidsurengiin Batbaatar*
Alan R. Gillespie
Quaternary Research Center, University of Washington, Seattle, Washington 98195-1310, USA

Michele Koppes
Department of Geography, University of British Columbia, Vancouver BC V6T 1Z2, Canada

Douglas H. Clark
Department of Geology, Western Washington University, Bellingham, Washington 98225-9160, USA

Oliver A. Chadwick
Department of Geography, University of California–Santa Barbara, Santa Barbara, California 93106, USA

David Fink
Australian Nuclear Science and Technology Organisation, New Illawarra Road, Lucas Heights, NSW 2234, Australia

Ari Matmon
The Fredy and Nadine Herrmann Institute of Earth Sciences, The Hebrew University of Jerusalem, Edmond J. Safra Campus Givat Ram, Jerusalem 91904, Israel

Summer Rupper
Department of Geography, University of Utah, Salt Lake City, Utah 84112, USA

ABSTRACT

Glaciers in central Asia that developed under a range of climatic conditions from arid to humid provide an excellent opportunity to test glacial responses to changes in climate. To do this, we mapped and dated glacial deposits at 11 sites spread over five mountain ranges in central Asia: the Altai, Tian Shan, Altyn Tagh, Qilian Shan, and Kunlun. The glacial chronologies for these sites were determined from new ^{10}Be and ^{26}Al exposure ages for the mapped moraines, in addition to ^{10}Be ages available in the literature. Paleo–equilibrium-line altitudes were estimated for past glacier extents from the dated moraines. The equilibrium-line altitudes (ELAs) were also estimated for existing glaciers to characterize the spatial pattern in modern climate across the study region. Differences between the modern and paleo-ELAs (ΔELAs) were used to explore the climatic reasons for variations in the glacier sensitivities and responses

*corresponding author email: bataa@uw.edu

Batbaatar, J., Gillespie, A.R., Koppes, M., Clark, D.H., Chadwick, O.A., Fink, D., Matmon, A., and Rupper, S., 2020, Glacier development in continental climate regions of central Asia, *in* Waitt, R.B., Thackray, G.D., and Gillespie, A.R., eds., Untangling the Quaternary Period: A Legacy of Stephen C. Porter: Geological Society of America Special Paper 548, https://doi.org/10.1130/2020.2548(07).

to past changes in climate. The results show that the glaciers in more humid regions advanced to their maximum during marine oxygen-isotope stage (MIS) 3–2 with ΔELAs of ~1100–600 m. However, glaciers in the arid interior of central Asia, in the rain shadows of the Karakorum and Pamir ranges and in the Gobi Desert ranges, reached their maximum between MIS 6 and 4, and glacier extents during the subsequent colder/drier MIS 3–2 were significantly smaller or did not extend beyond their cirques. Comparisons of our results and the sensitivity analysis of modern glaciers suggest that depression of air temperature was the primary driver of glacier advances in central Asia but that precipitation played a major role in shaping the spatial and temporal heterogeneity of glacier advances. Precipitation was especially important in hyperarid conditions. Therefore, inferences about paleoclimate parameters from past glacial extents must be made after careful consideration of the climatic setting in which the glaciers are found, as well as their sensitivity to climatic factors.

INTRODUCTION

The mass balance of a mountain glacier, the difference between accumulation of snow and ablation of glacier ice, is the most accurate quantity with which to define its growth. Because accumulation and ablation both respond to local climate conditions, the fluctuation of glacier mass balance is used to infer changes in climate, past and present. The forcing climate factors and the corresponding changes to the glacier mass balance can be measured and/or estimated at any point on a glacier. Such an exercise at the equilibrium-line altitude (ELA) of a glacier, an estimated altitude at which the annual accumulation and ablation are equal, provides the most useful measure connecting the glacier and climate. Stephen Porter (1975) recognized the significance of defining climate conditions at the ELA and provided one of the most comprehensive instructions on estimating the glacier ELA. Porter (2000) further refined ELA-estimation methods, in which he emphasized the importance of surveying ELAs for glaciers in various climate conditions to accurately reconstruct paleoclimate from glacial evidence.

Selection of Study Sites

Regional-scale reviews of modern and paleo-ELAs in Asia have covered Tibet and the Himalayas (e.g., Owen and Benn, 2005; Heyman, 2014), but this study focuses more broadly on central Asia (Fig. 1) because climatic conditions there range from hyperarid to semihumid. Central Asia is defined here not politically ("Central Asia"), as at the end of the nineteenth century, but as the largely arid region between the northern slopes of the Himalayas in the south and Siberia in the north and ranging from the eastern edge of the Tibetan plateau to the Caspian Sea ("central Asia"; Fig. S1 in the Supplemental Material[1]). The climate in the interior of central Asia is continental, characterized by low precipitation and cold winters (Peel et al., 2001). In winter, the Siberian low-temperature–high-pressure system extends south to the central Asian interior near ~40°N latitude (Araguás-Araguás et al., 1998). More than 50% of the annual precipitation falls in the summer (Sakai et al., 2015), brought by westerly winds and monsoons from the Indian and Pacific oceans (Fig. 1; Araguás-Araguás et al., 1998). In a simplistic scheme, central Asia can be divided into three zones in terms of the precipitation source: (1) monsoon-free interior regions; (2) monsoon-influenced interior regions; and (3) the Himalayas, influenced by the Indian monsoon (Fig. 1). We focused our study on the regions of central Asia where the influence of monsoonal precipitation is minimal because the uncertainty in the monsoon intensity complicates the paleoclimate inference from the glacial evidence. In other words, we established a pattern of glacial responses in regions with precipitation mostly sourced from the westerlies.

We report the results of cosmic-ray exposure dating of glacially deposited boulders in five mountain ranges of central Asia (Fig. 1), and the estimation of modern and paleo-ELAs. We chose these study sites to establish spatial and temporal patterns of glaciations in different climatic conditions. Such regional mapping of ELA depressions (ΔELAs), the difference between the modern and paleo-ELAs, may reveal two fundamental aspects for inferring paleoclimate from glacial evidence: (1) Such mapping may identify glaciers with different sensitivities to climate variables, such as precipitation, where ΔELAs are estimated under similar climate conditions; (2) it may also be used to reconstruct paleoclimate variables in different regions where ΔELAs are estimated for glaciers with similar sensitivities.

Framework for Paleoclimate Reconstruction

We analyzed our results in terms of a two-dimensional climatic subspace relating the most important factors controlling glacier advance and retreat—precipitation and air temperature. In order to accurately reconstruct these climate variables from glacial evidence, the sensitivity of glaciers to the climate variables

[1]Supplemental Material. Photos of samples, assessment of cosmogenic data quality, data tables, and references. Please visit https://doi.org/10.1130/SPE.S.12915743 to access the supplemental material, and contact editing@geosociety.org with any questions.

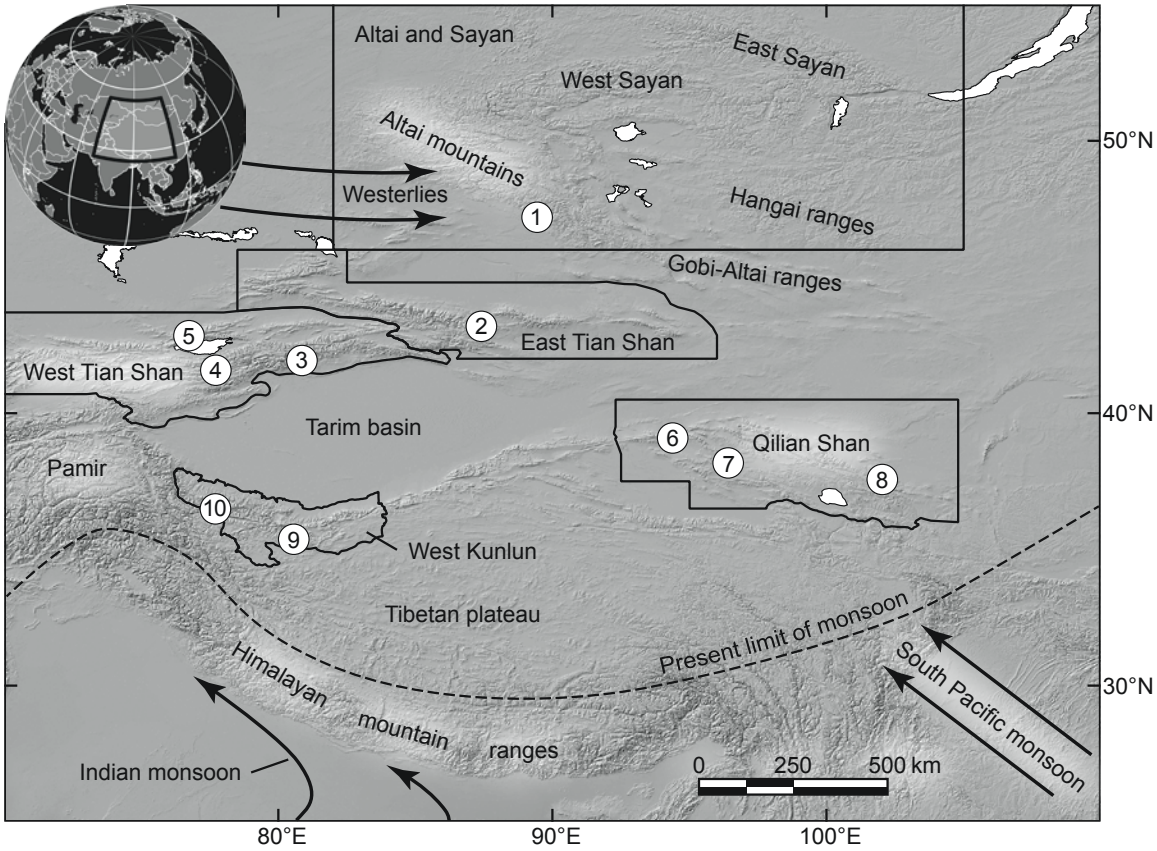

Figure 1. Study areas in central Asia with newly obtained ages: (1) Kax Kurta; (2) Diehanjelegou, Alashanje, and Daxigou; (3) Muzart and Tailan; (4) Suek, Barskoon, and Gulbel; (5) Choktal; (6) Altyn Tagh; (7) Dumda; (8) Gangshiqia; (9) Aksaiqin; and (10) Karakax. The delineation and the names of the regions were adopted from the second-order regions defined by the Randolph Glacier Inventory 6.0 (2017). The present limit of monsoonal precipitation from the Indian and South Pacific oceans is from Araguás-Araguás et al. (1998). The arrows indicate the general direction of major air flows (Benn and Owen, 1998). The shaded relief image was constructed from Shuttle Radar Topography Mission (SRTM) Digital Elevation Model (DEM) data (GTOPO030; U.S. Geological Survey, 2017).

must first be established. There are two general models that relate the ELA and climate: (1) empirical models of summer air temperature (T_{air}) and annual precipitation (*ppt*) at the ELA (e.g., Ohmura et al., 1992; Sakai et al., 2015); and (2) numerical models of ELA that account for various climate variables, including solar insolation (e.g., Mölg and Hardy, 2004; Rupper and Roe, 2008). An empirical curve constructed by Sakai et al. (2015), shown in Figure 2, demonstrates that the relationship between summer T_{air} and annual *ppt* at the ELA is not linear; in warmer climates, the ELA responds mostly to T_{air} changes, whereas in cold climates, the ELA becomes more sensitive to *ppt* than to T_{air}. The numerical models do not rely on the empirically established sensitivity. They can be used to calculate the heat transferred into and out of the glacier to estimate the ELA and can estimate the relative importance of various climate variables to the glacier mass balance. The numerical sensitivity model of Rupper and Roe (2008) shows that in humid environments, energy-efficient melt and subsequent runoff dominate glacier ablation and that changes in glacier mass balance are mainly sensitive to fluctuations in T_{air}. However, in cold and arid environments, sublimation by itself can ablate most of the accumulation, and the glacier mass balance may be more sensitive to changes in *ppt* (Fig. 2). These insights from the empirical and numerical models imply not only that glaciers with different sensitivities can respond differently to the same climate change, but also that the sensitivity of individual glaciers to T_{air} and *ppt* can change as conditions at the ELA fluctuate. The modern annual *ppt* in our study sites ranges from 1020 to 65 mm (Adler et al., 2003). The glaciers in these low-*ppt* continental climates are predicted to have wide-ranging sensitivities to *ppt* and T_{air} in the empirical and numerical models (e.g., Mölg and Hardy, 2004; Rupper and Roe, 2008; Sakai et al., 2015).

Chronostratigraphic Nomenclature and the Terms Used in This Study

We used the timing of the marine oxygen-isotope stages (MIS) constructed by Lisiecki and Raymo (LR04 stack: 2005)

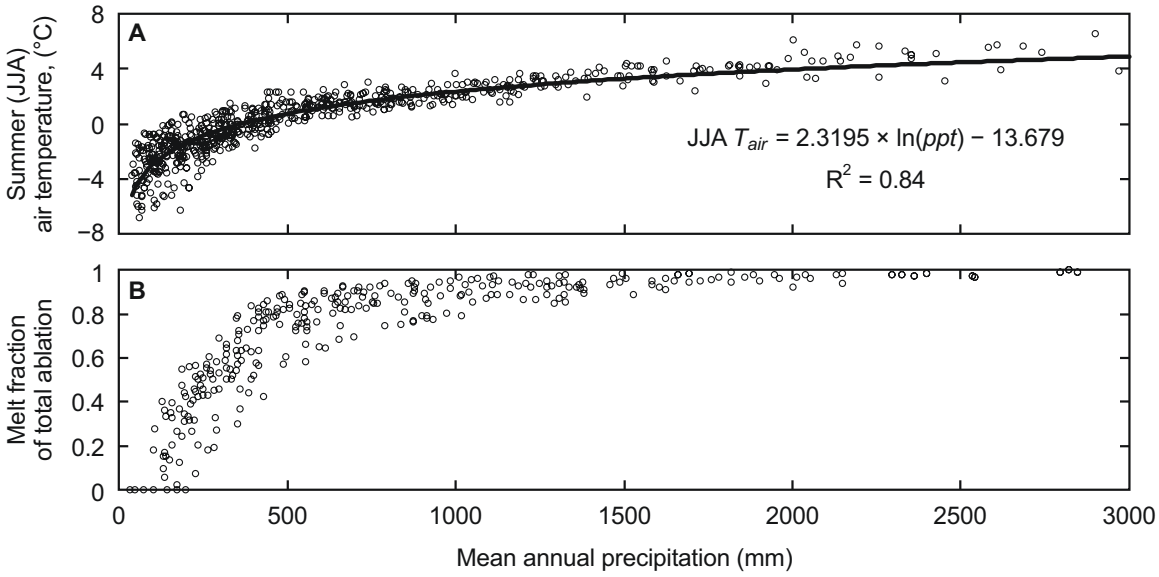

Figure 2. (A) Summer air temperature (June-July-August [JJA] T_{air}, °C) at the equilibrium-line altitude (ELA), showing 670 data points from Sakai et al. (2015). (B) Melt fraction of total ablation (308 data points from Rupper and Roe, 2008) for modern central Asian glaciers in regions with various annual precipitation values (*ppt*). The equation and the correlation coefficient (R^2) in the top panel were derived from a logarithmic fit (black line) between JJA T_{air} and annual *ppt*. Annual precipitation in the regions considered in this study ranged from 1020 to 65 mm.

as a broad stratigraphic nomenclature for the interpretations of our results, recognizing that the climate within these stages fluctuated and glaciers advanced and retreated on a finer temporal scale also. The LR04 stack integrated benthic $\delta^{18}O$ data recovered from 57 globally distributed sites to construct a single record of $\delta^{18}O$ fluctuations through time, and the stages were numbered in sequential order. The duration of the stages and their subdivisions, with an uncertainty of ±4000 yr, according to the LR04 stack are as follows: MIS 5: 130–71 ka; MIS 4: 71–57 ka; MIS 3: 57–29 ka; MIS 2: 29–14 ka; and MIS 1: 14–1 ka. The duration of the epochs mentioned in this paper were from the chronostratigraphic units defined by the U.S. Geological Survey Geological Names Committee (2010). We have used the term "local LGM" as the time when the largest glacier advance occurred at a particular site (where LGM indicates last glacial maximum), defined by lateral and end moraines observed in the field and from satellite and aerial images. The timing of local LGM could thus vary from place to place. In contrast, the term "global LGM" as used in this paper refers to a fixed period: 26.5–19 ka as defined by Clark et al. (2009) based on the timing of the maximum extents of ice sheets and mountain glaciers around the globe.

Concepts and Terms to Describe Sensitivity of ELA to Climate Variables

The relative contributions of melt and sublimation to the total ablation of modern central Asian glaciers calculated by Rupper and Roe (2008) provided the basis for the following two terms: (1) melt-dominated glaciers; and (2) sublimation-dominated glaciers. In this study, we refer to glaciers as melt-dominated if melt was responsible for more than 50% of total annual ablation. Sublimation-dominated glaciers can occur in hyperarid regions, where as much as 80 mm water equivalent of ice can be lost via sublimation annually (Batbaatar et al., 2018). In other words, the ratio of sublimation/melt can increase not only as precipitation decreases (constant T_{air}), but also with altitude: At higher, colder altitudes, a lower percentage of total ablation will be lost via melt. This altitude-dependent ratio of dominant ablation mechanisms is directly related to the ELA sensitivity to changes in T_{air} and *ppt*: If little melt occurs in subzero temperature conditions (and sublimation dominates ablation), then only *ppt* can drive accumulation, and hence the ELA. In this study, we refer to glaciers as temperature-controlled if more than 50% of the ΔELA can be explained by changes in T_{air}. Likewise, if change in *ppt* is responsible for more than 50% of the ΔELA, then we refer to these glaciers as precipitation-controlled glaciers.

METHODS

We sampled 94 boulders found on the crests of lateral and end moraines at 16 sites in five mountain ranges of central Asia: Altai, Tian Shan, Altyn Tagh, Qilian Shan, and Kunlun (Fig. 1). We also sampled four boulders sitting on alluvial fans, and three boulders and pebbles found on lake shorelines (Fig. 1). We measured concentrations of cosmogenic nuclides in the boulder samples and the four splits of the pebble sample (total 106 samples): 105 for ^{10}Be and 52 for ^{10}Be and ^{26}Al, to construct the glacial chronology in the study sites. Published boulder ages from lateral

and end moraines within the mountain ranges of the study sites (defined in Fig. 1) were also considered in order to establish the regional spatial and temporal pattern of glaciations. Throughout Mongolia, studied late Quaternary lake-level and ELA fluctuations have not been in phase (e.g., Grunert et al., 2000; Batbaatar et al., 2018), whether the modern lakes in closed basins are in relatively humid (e.g., Fedotov et al., 2004) or arid settings (e.g., Komatsu et al., 2001). Furthermore, global LGM lake levels were low, independent of the relative depression of the ELA locally, and in the most arid settings, lake levels rose early in the Holocene at the same time glaciers advanced (Batbaatar et al., 2018). We sought to compare the timing of Aksaiqin lake levels with the timing of the nearby glaciers in the hyperarid setting of the northwestern Tibetan plateau to investigate this relationship. Four splits of one sample of shoreline pebbles from Aksaiqin in the Kunlun were analyzed for ^{10}Be and ^{26}Al to see how the variability at the centimeter scale compared to the difference among terraces and to check how the timing of the high lake levels in this endorheic basin compared with large paleoglacier extents. We used the normalized deviation technique outlined by Batbaatar et al. (2018) to identify outlier ages. In order to approximate the glacier mass balance, we estimated the paleo-ELAs based on the dated and undated moraines. For comparison, the modern ELAs were also estimated using the same technique. The modern annual *ppt* and summer T_{air} were calculated using long-term gridded climate data sets. We then used the empirical curve constructed by Sakai et al. (2015), and the melt fractions of total ablation calculated by Rupper and Roe (2008) to infer paleoclimate conditions from the glacial evidence. Below, we describe the details of the modern climate data sets that we used, the cosmic-ray exposure dating, the procedures to identify outliers, the ELA estimation methods, and the glacier-sensitivity approximation.

Cosmic-Ray Exposure Dating and Outlier Evaluations

We followed the standard procedures for the exposure dating method: (1) Crush the sampled rocks to very coarse sand-sized pieces; (2) extract the quartz minerals from the sample by dissolving the other minerals in HF acid; (3) extract the Be and Al from the samples using column chromatography; (4) measure the isotope ratios, ^{10}Be/^{9}Be and ^{26}Al/^{27}Al, by accelerator mass spectrometry; and (5) calculate the ^{10}Be and ^{26}Al concentrations, accounting for the half-lives of the isotopes and the sample mass. The rock samples were prepared at the cosmogenic nuclide laboratories at the University of Washington, the University of Vermont, and the Hebrew University of Jerusalem. The Be ratios were measured at the ANTARES facility at the Australian Nuclear Science and Technology Organisation (Fink and Smith, 2007) against the standard known as 07KNSTD (Nishiizumi et al., 2007), and at the Center for Accelerator Mass Spectroscopy at the Lawrence Livermore National Laboratory (CAMS LLNL) using the standard known as KNSTD with a different nominal value of ^{10}Be/^{9}Be than 07KNSTD (Nishiizumi et al., 2007). The Al ratios were measured at CAMS LLNL using the standard KNSTD (Nishiizumi, 2004). The exposure ages were calculated using the CRONUS-Earth online calculator (Balco et al., 2008), version 2.3, with ^{10}Be and ^{26}Al production rates by Borchers et al. (2016). The cosmic-ray shielding factor was calculated in the CRONUS-Earth calculator using horizon-angle measurements made in the field. The density of the samples was assumed to be 2.65 g cm^{-3}. We used the exposure ages based on the constant production rate model with the spallation scaling scheme of Lal (1991) and Stone (2000), which is termed "St" in the online calculator (Balco et al., 2008). The ages calculated using the same scaling scheme that accounts for paleomagnetic changes (termed "Lm" in the online calculator) were similar to the ages calculated using the St scheme: ~70% of the time, the ages were within 5% of each other, and the ages with 10%–15% difference were either very young (<0.5 ka) or very old (>100 ka). The other three scaling schemes available in the online calculator, version 2.3, were deemed obsolete due to uncertainty in the use of modern cosmic-ray fluxes for cosmogenic nuclide production in rocks (Balco et al., 2008; Balco, 2016), and we did not use them to calculate the ages. For samples with measurements of both Be and Al concentrations, the difference between ^{10}Be and ^{26}Al ages was not large, averaged at ~12% of the ^{10}Be ages calculated for the sample. This age difference was similar to the mean external uncertainties of ~11% for ^{10}Be and ~13% for ^{26}Al ages that account for both analytical error and production rate scaling. Therefore, we based our glacial chronology in the study sites on the ^{10}Be ages to be compatible with the ^{10}Be ages available in the literature. However, we describe in detail in the Results section when ^{10}Be and ^{26}Al ages showed significant differences for an individual sample.

We used the literature data compiled by J. Heyman (2018, http://expage.github.io) to recalculate the exposure ages available in the studied mountain ranges. We followed the normalized deviation method of Batbaatar et al. (2018) to identify outliers in the new and recalculated literature ages. This method compares an individual age and its analytical (internal) uncertainty with the mean of the remaining ages in the group, using Equation 1:

$$\delta_i = \frac{|x_i - \mu_{n-i}|}{\sqrt{std_{n-i}^{\,2} + \sigma_i^{\,2}}}, \quad (1)$$

where δ_i is the normalized deviation for the age being tested, x_i, among n number of samples, μ_{n-i} is the mean of the group excluding x_i, std_{n-i} is the 1σ standard deviation of the group excluding x_i, and σ_i is the 1σ analytical uncertainty of x_i. An outlier is identified if $\delta_i > 2$. After rejecting the outliers, we calculated the mean of the remaining ages and compounded the 1σ standard deviation and 1σ external uncertainties of the remaining ages to derive 1σ total uncertainty of the age group. If an age group had only two samples, we simply calculated the mean of the ages and derived the total uncertainty the same way described above. No matter the number of samples in a group, if the total uncertainty of the group exceeded 50% of the mean, the mean age was deemed unreliable and was excluded from the ELA analysis and the related interpretations. We also used the statistical tests of Chauvenet (1891)

and Peirce (Ross, 2003) to check the robustness of the normalized deviation method and to provide comparison to studies that used Chauvenet's and Peirce's criteria. The normalized deviation method identified at least one outlier in 79% of the age groups considered in this study, whereas Chauvenet's and Peirce's tests identified outliers in 9% and 25% of the total number of age groups, respectively. The full references to the literature data used in this study and a detailed discussion on the assessment of quality of the cosmogenic data are provided in the Supplemental Material (see footnote 1).

We carefully examined boulders in the field to look for any evidence of burial and sampled from the top of the boulders to avoid eroded or exhumed surfaces to the extent possible. The reported ages assume no erosion and burial, but we acknowledge that was not true in some cases. We provide representative photos of the eroded boulders and moraine surfaces in the Supplemental Material and discuss the limitations in the interpretation of the ages for the eroded boulders in the Results section. The younger boulders were not visibly eroded, and representative photos of them are also included in the Supplemental Material. An unlikely boulder erosion of 3 mm yr^{-1} would increase an apparent age of 50 ka by 15% or an apparent age of 20 ka by 5%, which was not large enough to change our interpretation (Fig. S2 [see footnote 1]). Batbaatar and Gillespie (2016) estimated that shielding by a 4 mo seasonal snowpack of 250 mm depth would increase an apparent age of 20 ka by ~2%, similar to the analytical uncertainty for ^{10}Be ages. We report the exposure ages, recognizing that they represent minima for the dated landforms.

The basic assumption in using cosmogenic nuclides for dating glacial boulders is that the accumulation of cosmogenic nuclides starts at a time when the boulder is deposited by a glacier and exposed to the sky. The freshly plucked boulders are carried downhill by the glacier until local ablation exceeds accumulation, and the boulders are deposited on the crests of terminal and lateral moraines. According to Anderson et al. (2014), many moraines appear to have formed within ~50 yr, a period appropriate to be representative of climate calculated from the interannual variables of weather. Therefore, we assumed that the paleoglaciers were in equilibrium with climate when they formed the moraines, and the boulders we sampled from the moraine crests represent a time when the paleoglacier was in standstill. In other words, our reported mean group ages after rejecting outliers do not uniquely reflect the timing of glacier advance or the onset of deglaciation.

Equilibrium-Line Altitude

By definition, the ELA of glaciers is situated on the glacier surface where annual accumulation and ablation are equal, and the ELA is a direct proxy for annual mass balance. An accurate inference about climate from ELAs then has to be derived from the annual ELAs averaged over the time period of climate statistics (e.g., ≥30 yr). In our study, we defined the estimated paleo-ELAs from moraine locations as this "climate ELA." Above, we defined that the exposure ages for the moraines represent the time of glacier standstills, and the paleo-ELAs estimated from the dated moraines are therefore interpreted as the local climate ELA for glaciers in equilibrium with climate. However, in the absence of annual measurements of glacier mass balance or the glacier itself, the mass balance ELA was approximated by geometric ELAs estimated using empirical constraints.

There are many ways to estimate the ELA, of which the toe-headwall altitude ratio (THAR) and accumulation-area ratio (AAR) methods are the most reliable (e.g., Porter, 1975, 2000; Meierding, 1982; Benn and Lehmkuhl, 2000; Benn et al., 2005; Heyman, 2014). The AAR approach assumes that the accumulation area covers a certain fraction of the total area of the glacier (~65% for most temperate, debris-free glaciers; Porter, 2000), and measurement of this fraction requires accurate estimations of glacier outline. We did not use the AAR method due the lack of constraints on the outlines of dated paleoglaciers. Instead, we used the simpler *THAR* method to estimate the ELAs using Equation 2:

$$ELA = A_t + THAR(A_h - A_t), \quad (2)$$

where A_t is toe altitude, A_h is headwall altitude, and *THAR* is a threshold value unique to a glacier. For modern glaciers, we used outlines provided in the Randolph Glacier Inventory 6.0 (RGI Consortium, 2017), and the toe altitudes were measured from Google Earth (2017). For paleoglaciers, the minimum altitude of a moraine, measured in the field and from Google Earth, was taken to approximate the toe altitude. The altitudes of bergschrunds visible on Google Earth were approximated as the headwall altitudes for modern glaciers. For paleoglacier headwall altitudes, however, we estimated a value from three altitudes above the glaciated valley: (1) at one third of the altitude difference between the cirque floor and the peak; (2) at the point where avalanche chutes end in free air above the cirque floor, assuming that the glacier shielded the rocks below from erosion; and (3) at the highest peak, in cases where glacial horns, arêtes, or cols did not exist. We assumed that the paleoglaciers in the same valley shared the same headwall, which made the *THAR* ELAs sensitive only to the toe altitudes.

Our approach followed the methods used by Batbaatar et al. (2018), who noted that potentially one of the greatest sources of uncertainty in the ELA estimation was the selection of a threshold *THAR* value. We estimated the modern and paleo-ELAs using *THAR* values of 0.6 and 0.58 for sites in Mongolia following Gillespie et al. (2008) and Batbaatar et al. (2018). In high-relief areas, an ~2000 m difference between the toe and headwall altitudes would lead to an ELA difference of ~200 m, depending on the choice of a threshold *THAR* value of 0.5 or 0.6, and the corresponding ΔELA values would differ by ~130 m. However, only ~20% of the local glacial maximum established in this study exhibited >1500 m difference in toe and headwall altitudes. The majority of the paleoglaciers considered in this study were less extensive, and the precision of their *THAR* ELAs approached

the precision of ~100 m, similar to the ELA accuracy estimated for the Sierra Nevada glaciers in the western United States (Gillespie, 1991).

The accuracy of the *THAR* ELA depends on the accurate reconstruction of the glacier extent, and we used only lateral and end moraines for the ELA analysis. The crests of the lateral and end moraines were identified and mapped in the field and from Advanced Spaceborne Thermal Emission and Reflection Radiometer (ASTER; NASA and METI, 2001), declassified DISP/KH-9 (U.S. Geological Survey, 2018a), and Google Earth images for the new study sites. In some cases, where old moraines exhibited less clear ridges compared to young moraines, we mapped the highest points on the moraines, usually in the middle of the ridges, as moraine crests. We examined the original maps provided in the literature for each published age we used in our study and cross-examined the moraine surfaces using Google Earth to confirm the moraine crests. Published ages for surfaces that did not determine the glacier extent (e.g., bedrocks, landslides, and rock glaciers) were not considered for ELA analysis.

We also used the maximum elevation of lateral moraines (MELM) as minimum estimates for the local ELAs (Porter, 2000) where the dated lateral moraines did not fit morphologically with the end moraines, or where recognizable end moraines simply did not exist. The precision of the MELM ELA must be approximated from the accuracy of the global positioning system (GPS) unit (~10 m) and the vertical uncertainty of the terrain data. The RGI 6.0 inventory uses ASTER Global Digital Elevation Model (GDEM; NASA and METI, 2017) data, and Google Earth uses Shuttle Radar Topography Mission (SRTM) data for altitude, in which both elevation data have a vertical uncertainty of 30 m.

The estimated modern and paleo-ELAs were mapped on a regional scale using QGIS, version 2.12.1-Lyon (https://www.qgis.org) and the "Contour" plugin tool developed by Lionel Roubeyrie and Chris Crook (https://github.com/ccrook/QGIS-Contour-Plugin). The modern and paleo-ELA values and the coordinates necessary to reproduce the maps are available in the Supplemental Material (see footnote 1).

Normalized ELA Depression

Modern glaciers in central Asia have been predicted to exhibit large spatial variations in sensitivities (Rupper and Roe, 2008). In the past and under a different climate, their ELAs might have exhibited a different pattern of spatial variation, one that might have led to the maximum local LGM occurring at different times from range to range. This glacial asynchrony, in both spatial and temporal senses, can be examined by normalizing the local ELAs to the headwall altitude (A_h) and plotting the values in a time series. We followed the approach of Batbaatar et al. (2018) to calculate the normalized ELA depression, ΔELA_{norm} (dimensionless), using Equation 3:

$$\Delta ELA_{norm} = \frac{A_h - ELA_{dated}}{A_h - ELA_{min}}, \quad (3)$$

where ELA_{dated} is an ELA estimated from a dated moraine, and ELA_{min} is the lowest ELA within a valley, estimated from the lowest moraine regardless of whether the moraine was dated or not. Therefore, ELA_{min} represents the spatial magnitude of the local LGM standstill. When ELA_{dated} corresponds to $\Delta ELA_{norm} = 1$, the moraine age represents the timing of the local LGM. The ΔELA_{norm} can be a useful basis for visualization to decipher the reasons for the spatial and temporal variations of glacier advances.

Climate at the Modern ELAs

We characterized the modern long-term values of climate variables based on the following data sets: (1) monthly surface (2 m above ground) T_{air} at the altitude of the gridded cells with 0.5° resolution (based on GTOPO30; U.S. Geological Survey, 2017) from Global Historical Climatology Network version 2 and Climate Anomaly Monitoring System (GHCN CAMS; Fan and van den Dool, 2008); (2) annual *ppt* grids with 2.5° resolution from the Global Precipitation Climatology Project (GPCP, version 2.3; Adler et al., 2003); and (3) monthly T_{air} lapse rate grids with 2.5° resolution from reanalysis data produced by the National Center for Environmental Prediction and the National Center for Atmospheric Research (NCEP/NCAR reanalysis version 1; Kalnay et al., 1996). The long-term monthly mean values of climate variables in all of these climate data sets were calculated from data covering 1981–2010. We calculated the summer values of T_{air} and the lapse rate by averaging the June, July, and August (JJA) values for the grids where the study sites occur. The glacier altitudes used for the estimation of the modern ELAs were taken from the Randolph Glacier Inventory (RGI) 6.0 (RGI Consortium, 2017) and from Google Earth. The delineations of the mountain ranges were from Global Terrestrial Network for Glaciers (GTN-G, 2017), and the identification numbers for modern glaciers followed the RGI 6.0. The local names of the valleys and peaks were based on the interviews with local people and published literature.

Sensitivity of Modern Glaciers in Central Asia

Glacier ablation can be expressed as a function of altitude because it depends on the heat exchange between the surface of the glacier and the atmosphere, which attenuates with altitude (Rupper, 2007). T_{air} and insolation are the significant regulators of ablation and, together with *ppt*, can be used to define the climatic conditions at the ELA (e.g., Rupper and Roe, 2008). Ohmura et al. (1992) constructed summer T_{air} (proxy for ablation) and annual *ppt* (proxy for accumulation) values at the ELA to empirically establish the relationship between these two important climate variables. Rupper and Roe (2008) found that in high-precipitation regions, T_{air} was the most effective regulator of glacier mass balance. We therefore focused on two climate variables in this study, T_{air} and *ppt*.

Vargo et al. (2018) used a numerical model to calculate the spatial variation of ablation for modern Andean glaciers. They

quantified the ELA sensitivities to T_{air}, *ppt*, and solar insolation, finding that the ELA sensitivity to T_{air} (the change in ELA for a unit change in T_{air}: $\partial ELA/\partial T_{air}$) was ~180 m °C^{-1} regardless of the local *ppt*. However, the ELA sensitivity to annual *ppt* (the change in ELA for a percent change in modern *ppt*: $\partial ELA/\partial ppt$) was greater in hyperarid regions than in more humid regions, and $\partial ELA/\partial ppt$ gradually decreased as the accumulation increased. Such parametrized sensitivity calculations have not been completed for central Asia. Shea and Immerzeel (2016) compiled ΔELA data from high-altitude regions around the world to derive an empirical equation to estimate $\partial ELA/\partial T_{air}$ in relation to annual *ppt*:

$$\partial ELA/\partial T_{air} = 16.46(ppt–379.61)^{0.32}. \quad (4)$$

Equation 4 mathematically does not permit the calculation of $\partial ELA/\partial T_{air}$ if the *ppt* is below ~380 mm, because *ppt* in the regions considered by Shea and Immerzeel (2016) ranged from 3000 to 410 mm. This approach was successfully used in the calculations of glacier recessions in the Himalayas and Hindu Kush under various warming climates (Kraaijenbrink et al., 2017) because annual *ppt* there permits the use of Equation 4. However, annual *ppt* in most of our study sites was below 410 mm. Glaciers in such cold and arid regions are expected to be more sensitive to *ppt* than to T_{air} (Rupper and Roe, 2008; Sakai et al., 2015).

We used melt fraction values of Rupper and Roe (2008) to qualitatively characterize the modern glaciers as sensitive to T_{air} or *ppt* for each valley with new and published glacial chronologies. Most of the studied valleys host modern glaciers in their cirques, but in the absence of a modern glacier, we approximated the modern ELA (above the cirque headwall) from the ELA of the nearest glacier with the same aspect as the studied valley. Although the melt fraction of Rupper and Roe (2008) is related to the ELA sensitivities to T_{air} and *ppt*, we note that their proportionalities are unknown, and quantified approximations of the sensitivities should not be made from the melt fraction.

RESULTS

The mountain ranges considered in this study cover ~715,000 km^2. We studied one valley in the Altai range, three valleys in the East Tian Shan, five valleys in the West Tian Shan, three separate mountain ranges within the broader Qilian Shan, and three glaciated valleys in the West Kunlun. The exposure age results (Tables 1–2; Tables S1–S3 [see footnote 1]) are organized by the mountain ranges where the study sites are located. The outlier evaluations for grouped ages with more than three samples are provided in Tables S4–S6 (see footnote 1). The mean ages for the age groups with two samples are summarized in Table S7 (see footnote 1). For each site, we report the new exposure ages along with the modern and paleo-ELA results (Tables S8–S9 [see footnote 1]). We also describe the modern climate conditions at the modern ELA (Table S10 [see footnote 1]). We follow these descriptions with the recalculated exposure ages from literature, with further discussion of our interpretation of the new and literature ages. We provide the paleoclimate inferences based on the reconstruction of the dated paleo-ELAs within each mountain range at the end of the section.

Altai Range, Kax Kurta

Stretching over 1000 km in an approximately NW-SE direction, the Altai range spans the borders between Russia, Mongolia, and China (#1 in Fig. 1). Our study site, Kax Kurta valley, is located in the southeastern part of the range (Fig. 3). The altitude of the highest peak in the vicinity is ~3220 m above sea level (m asl), and it hosts a small (perennial?) snowfield in a sheltered part of the SW-facing cirque. The Kax Kurta valley is unglaciated now. We sampled two moraines within the ~2.7-km-wide valley. Two boulders from an end moraine closest to the cirques (Fig. 3) gave a mean ^{10}Be age of 17.3 ± 2.4 ka, corresponding to *THAR* ELA of 2970 m asl. Approximately 5 km down valley, an undated, well-preserved end moraine gave a *THAR* ELA of ~2840 m asl. About ~1.5 km farther down valley, we collected a single boulder from a left-lateral moraine that gave a ^{10}Be age of 21.6 ± 2.5 ka and an ^{26}Al age of 22.5 ± 2.4 ka. Despite this agreement, we cannot confidently constrain the age of this moraine from a single sample. This lateral moraine was probably deposited by the largest paleoglacier in the valley with a *THAR* ELA of ~2760 m asl. The nearest modern glacier with NW cirque orientation similar to the Kax Kurta cirque can be found ~50 km to the north. This modern glacier had a *THAR* ELA of ~3570 m asl (*ppt* ~200 mm and summer T_{air} = 4 ± 1.1 °C at the ELA), which was higher than the headwalls of the Kax Kurta paleoglacier. Approximately 260 km to the NW, Gribenski et al. (2018) sampled the three lowest moraines in the Kanas valley and dated them to ca. 21–18 ka with a *THAR* ELA of ~2510 m asl.

Another 120 km to the NE, Reuther et al. (2006), Reuther (2007), and Gribenski et al. (2016) dated a series of end and lateral moraines in the Chagan Uzun valley. The left-lateral moraines on the northern walls of the valley were deposited ca. 26–18 ka, corresponding to a MELM ELA of ~2640–2330 m asl. The boulders on the lower end moraines gave a mean age of 18.8 ± 3.8 ka with *THAR* ELA of ~2920 m asl.

East Tian Shan, Diehanjelegou

The study site, Diehanjelegou valley (Fig. 4), is located in the SE corner of the East Tian Shan, which spans ~360 km in the NW-SE direction. We sampled four boulders from a right-lateral moraine on the piedmont at the mouth of the valley, which gave a mean ^{10}Be age of 31.9 ± 10.8 ka. One of the samples in this group, XCS-104, yielded a significantly greater ^{26}Al age (43.3 ± 4.5 ka) than the ^{10}Be age (30.0 ± 3.0 ka), implying an analytical error in the measurements of the ^{26}Al concentration, although the ages overlap within 2σ external uncertainty. Two boulders from the left-lateral moraine at a similar altitude gave a mean ^{10}Be age of 30 ± 12.9 ka. Both of these moraines can be traced to an end

TABLE 1. DATA FOR COSMOGENIC NUCLIDE ANALYSIS

Site	Sample	Location (°N, °E)	Elevation (m asl)	Thickness (cm)	Shielding factor	Quartz* (g)	Be carrier (mg)	$^{10}Be/^{9}Be$ ($\times10^{-15}$)	^{10}Be concentration ($\times10^{3}$ atoms g^{-1} SiO_2)	^{10}Be standard†	^{26}Al concentration§ ($\times10^{3}$ atoms g^{-1} SiO_2)	^{26}Al standard#
Kax Kurta	XCS-120a	47.46109, 89.87250	2794	5.0	0.97	—	—	—	625.2 ± 26.6	KNSTD	4447.8 ± 294.8	KNSTD
Kax Kurta	XCS-120b	47.46109, 89.87250	2794	5.0	0.97	—	—	—	660.4 ± 26.1	KNSTD	3770.7 ± 280.1	KNSTD
Kax Kurta	XCS-121	47.46111, 89.79944	2486	10.0	1.00	—	—	—	648 ± 50.9	KNSTD	4114.5 ± 244.5	KNSTD
Diehanjelegou	XCS-101	43.15883, 87.44098	3080	5.0	1.00	—	—	—	1590.1 ± 54.2	KNSTD	9823.2 ± 460.1	KNSTD
Diehanjelegou	XCS-102	43.15901, 87.44026	3122	5.0	1.00	—	—	—	907.3 ± 33	KNSTD	5284.9 ± 266.2	KNSTD
Diehanjelegou	XCS-103	43.15751, 87.45024	3014	5.0	1.00	—	—	—	2191.9 ± 71.9	KNSTD	12,180.8 ± 571.3	KNSTD
Diehanjelegou	XCS-104	43.15690, 87.44908	3025	5.0	1.00	—	—	—	1195.5 ± 65	KNSTD	10,412.5 ± 553.3	KNSTD
Diehanjelegou	XCS-105	43.15690, 87.44908	3025	5.0	1.00	—	—	—	1669.3 ± 82.2	KNSTD	10,667.8 ± 564.5	KNSTD
Diehanjelegou	XCS-106	43.15690, 87.44908	3025	5.0	1.00	—	—	—	952.1 ± 30	KNSTD	6062.8 ± 277.8	KNSTD
Alashanje	CS-111a	42.92695, 86.87829	3267	2.5	1.00	—	—	—	3874 ± 105.4	KNSTD	24,188.3 ± 1139.8	KNSTD
Alashanje	CS-111b	42.92695, 86.87829	3267	2.5	1.00	—	—	—	2386.9 ± 73.7	KNSTD	15,411.7 ± 794.7	KNSTD
Alashanje	CS-112	43.02119, 86.97594	3658	5.0	0.99	—	—	—	1067.1 ± 72	KNSTD	6991.4 ± 589.8	KNSTD
Daxigou	CS-10	43.11882, 86.92159	3181	8.0	0.97	—	—	—	639.5 ± 29.3	KNSTD	—	—
Daxigou	CS-11b	43.11040, 86.94462	3021	8.0	0.97	—	—	—	873.4 ± 35.7	KNSTD	—	—
Daxigou	CS-12a	43.11040, 86.94462	2992	8.0	0.97	—	—	—	717.8 ± 37.5	KNSTD	4592.8 ± 286.2	KNSTD
Daxigou	CS-5	43.11586, 86.82338	3718	5.0	0.97	—	—	—	20.4 ± 11.2	KNSTD	—	—
Daxigou	CS-6	43.11586, 86.82338	3718	5.0	0.97	—	—	—	86.5 ± 12.8	KNSTD	—	—
Daxigou	CS-7b	43.11556, 86.84138	3592	5.0	0.99	—	—	—	917.3 ± 40.9	KNSTD	5161.4 ± 374.7	KNSTD
Daxigou	CS-8	43.11951, 86.92004	3417	1.0	0.99	—	—	—	957.4 ± 44.6	KNSTD	5415.1 ± 333.4	KNSTD
Muzart	CS-28	41.78571, 80.90608	1978	4.0	1.00	—	—	—	303.1 ± 23.6	KNSTD	2183.2 ± 41.4	KNSTD
Muzart	CS-30	41.79149, 80.90501	2011	4.0	1.00	—	—	—	334.3 ± 19.7	KNSTD	1800.3 ± 133.2	KNSTD
Muzart	CS-32	41.77471, 80.95658	1889	4.0	1.00	—	—	—	336.5 ± 16.5	KNSTD	—	—
Muzart	CS-33	41.77288, 80.95874	1874	2.0	1.00	—	—	—	465.9 ± 75	KNSTD	—	—
Tailan	CS-14	41.60214, 80.48376	1677	6.0	1.00	—	—	—	97.7 ± 11.2	KNSTD	463.1 ± 37	KNSTD
Tailan	CS-20	41.65480, 80.45959	2053	5.0	1.00	—	—	—	262.4 ± 16	KNSTD	1391 ± 86.5	KNSTD
Tailan	CS-24	41.63056, 80.46984	1879	3.0	1.00	—	—	—	161.6 ± 25.6	KNSTD	1160 ± 107.5	KNSTD
Tailan	CS-27a	41.54257, 80.48545	1565	5.0	1.00	—	—	—	95.3 ± 10.5	KNSTD	361 ± 41.4	KNSTD
Barskoon	BS-001A	41.88323, 77.70568	3822	2.0	1.00	11.338	0.2711	10.30 ± 1.50	16.5 ± 3.4	07KNSTD	—	—
Barskoon	BS-002A	41.88323, 77.70568	3822	2.0	1.00	14.826	0.2752	22.20 ± 3.1	27.5 ± 5.5	07KNSTD	—	—
Barskoon	BS-002B	41.88323, 77.70568	3822	2.0	1.00	15.68	0.2697	15.50 ± 2.10	17.8 ± 3.4	07KNSTD	—	—
Barskoon	BS-004A	41.88288, 77.70610	3831	3.0	1.00	14.097	0.2711	51.20 ± 4.60	65.8 ± 8.4	07KNSTD	—	—
Barskoon	BS-007A	41.87017, 77.73407	3791	3.0	1.00	13.667	0.2766	636.20 ± 9.90	860.4 ± 22.5	07KNSTD	—	—
Barskoon	BS-007B	41.87017, 77.73407	3791	5.0	1.00	15.077	0.2599	726.50 ± 10.50	836.8 ± 20.8	07KNSTD	—	—
Barskoon	BS-007C	41.86975, 77.73563	3805	2.0	1.00	16.131	0.2724	908.90 ± 25.30	1025.6 ± 42.9	07KNSTD	—	—
Barskoon	BS-007D	41.86975, 77.73563	3805	1.0	1.00	16.201	0.2655	626.00 ± 40.20	685.5 ± 63	07KNSTD	—	—
Suek	SO-CS-001	41.70825, 77.80538	3432	3.0	1.00	9.819	0.2349	555.80 ± 12.60	888.5 ± 31.1	07KNSTD	—	—
Suek	SO-CS-002A	41.70142, 77.81050	3402	2.0	1.00	9.416	0.2711	322.30 ± 8.60	620.1 ± 25	07KNSTD	—	—
Suek	SO-CS-002B	41.70142, 77.81050	3402	5.0	1.00	10.307	0.246	585.60 ± 15.30	933.9 ± 37	07KNSTD	—	—
Gulbel	GP-001	42.03892, 77.12420	2803	3.0	1.00	13.345	0.2808	338.10 ± 19.80	475.4 ± 39.9	07KNSTD	—	—
Gulbel	GP-002C	42.01070, 77.19833	3258	5.0	0.99	13.487	0.2613	485.22 ± 14.80	628.2 ± 28.5	07KNSTD	—	—
Gulbel	GP-002D	42.01238, 77.20202	3208	3.0	0.99	12.341	0.2808	435.76 ± 8.15	662.5 ± 19.9	07KNSTD	—	—
Gulbel	GP-003A	42.01432, 77.19927	3265	3.0	1.00	12.829	0.2641	519.70 ± 13.20	714.9 ± 27.6	07KNSTD	—	—
Gulbel	GP-003B	42.01432, 77.19927	3265	3.0	1.00	14.079	0.2738	514.90 ± 21.10	669.1 ± 39.9	07KNSTD	—	—
Gulbel	GP-003C	42.01447, 77.19822	3252	3.0	1.00	12.421	0.2766	492.30 ± 7.40	732.6 ± 18.7	07KNSTD	—	—
Gulbel	GP-004A	42.03813, 77.14208	3001	3.0	1.00	12.132	0.2613	321.30 ± 11.90	462.4 ± 25.1	07KNSTD	—	—

(*Continued*)

TABLE 1. DATA FOR COSMOGENIC NUCLIDE ANALYSIS (*Continued*)

Site	Sample	Location (°N, °E)	Elevation (m asl)	Thickness (cm)	Shielding factor	Quartz* (g)	Be carrier (mg)	$^{10}Be/^{9}Be$ ($\times10^{-15}$)	^{10}Be concentration ($\times10^{3}$ atoms g^{-1} SiO_2)	^{10}Be standard†	^{26}Al concentration§ ($\times10^{3}$ atoms g^{-1} SiO_2)	^{26}Al standard#
Gulbel	GP-004B	42.03813, 77.14208	3001	3.0	1.00	10.725	0.2627	1045.70 ± 32.40	1711.5 ± 78.8	07KNSTD	—	—
Gulbel	GP-005	42.03828, 77.12057	2781	1.0	1.00	12.278	0.2613	479.60 ± 8.50	682 ± 19.6	07KNSTD	—	—
Gulbel	GP-006	42.03822, 77.12402	2798	2.0	1.00	11.82	0.2655	447.60 ± 8.50	671.8 ± 20.4	07KNSTD	—	—
Choktal	CR-001A	42.70139, 76.70089	3197	3.0	1.00	9.547	0.3016	417.30 ± 7.68	880.9 ± 26.1	07KNSTD	—	—
Choktal	CR-001B	42.70139, 76.70089	3197	5.0	1.00	9.85	0.2738	497.21 ± 10.54	923.5 ± 30.6	07KNSTD	—	—
Choktal	CR-001C	42.70139, 76.70089	3197	3.0	1.00	10.858	0.2794	487.76 ± 8.88	838.7 ± 24.6	07KNSTD	—	—
Choktal	CR-002A	42.74965, 76.69540	3574	3.0	0.98	10.886	0.2655	7.51 ± 1.23	12.2 ± 2.8	07KNSTD	—	—
Choktal	CR-002D	42.75083, 76.69513	3588	3.0	0.97	10.423	0.2655	7.32 ± 1.52	12.5 ± 3.7	07KNSTD	—	—
Choktal	CR-002E	42.75083, 76.69513	3588	3.0	0.97	10.949	0.2711	7.23 ± 1.16	12 ± 2.7	07KNSTD	—	—
Choktal	CR-003A	42.74775, 76.69392	3535	10.0	0.98	10.487	0.246	437.75 ± 8.97	686.2 ± 22.1	07KNSTD	—	—
Choktal	CR-003C	42.74775, 76.69392	3535	5.0	0.98	11.758	0.2572	484.10 ± 9.05	707.6 ± 21.2	07KNSTD	—	—
Choktal	CR-003D	42.74707, 76.69433	3534	5.0	0.98	11.002	0.2863	425.24 ± 8.46	739.4 ± 23.3	07KNSTD	—	—
Altyn Tagh	CAT-02C	39.31450, 93.74186	4401	3.0	0.92	15.757	0.2446	89.87 ± 5.53	93.2 ± 8.2	07KNSTD	—	—
Dumda	CH-DU-01	37.85994, 96.28808	4039	1.0	1.00	8.98	0.246	3779.00 ± 44.20	6917.6 ± 150.5	07KNSTD	—	—
Dumda	CH-DU-02	37.85203, 96.28636	4036	1.0	1.00	6.872	0.2446	3642.30 ± 53.29	8663 ± 217.1	07KNSTD	—	—
Dumda	CH-DU-03	37.86278, 96.28833	4056	1.0	1.00	7.135	0.2475	3294.90 ± 56.41	7637.4 ± 214.1	07KNSTD	—	—
Gangshiqia	QS-GG-001	37.69356, 101.45208	4085	3.0	1.00	7.89	0.246	313.30 ± 7.59	652.7 ± 24.2	07KNSTD	—	—
Gangshiqia	QS-GG-002	37.69356, 101.45208	4085	1.0	1.00	16.474	0.2446	798.94 ± 15.72	792.7 ± 24.7	07KNSTD	—	—
Gangshiqia	QS-GG-003	37.69417, 101.45319	4101	5.0	1.00	16.251	0.246	821.64 ± 17.08	831.1 ± 27.1	07KNSTD	—	—
Gangshiqia	QS-GG-004	37.69417, 101.45319	4101	5.0	1.00	14.127	0.2446	735.81 ± 12.77	851.3 ± 24.1	07KNSTD	—	—
Gangshiqia	QS-GG-005	37.69417, 101.45319	4120	4.0	1.00	8.378	0.246	114.09 ± 4.86	223.9 ± 13.9	07KNSTD	—	—
Gangshiqia	QS-GG-006	37.69444, 101.45417	4120	6.0	1.00	8.412	0.2446	91.94 ± 3.59	178.6 ± 10.2	07KNSTD	—	—
Gangshiqia	QS-GG-007	37.69111, 101.45194	4041	3.0	1.00	12.568	0.246	525.60 ± 11.93	687.5 ± 24.1	07KNSTD	—	—
Gangshiqia	QS-GG-008	37.66339, 101.42669	3615	4.0	0.99	12.229	0.246	613.17 ± 20.43	824.2 ± 40.5	07KNSTD	—	—
Gangshiqia	QS-GG-009	37.66339, 101.42669	3615	3.0	0.99	9.306	0.246	444.50 ± 9.09	785.2 ± 25.3	07KNSTD	—	—
Gangshiqia	QS-GG-010	37.66050, 101.42356	3556	3.0	1.00	4.026	0.246	158.95 ± 6.44	649 ± 38.3	07KNSTD	—	—
Gangshiqia	QS-GG-011	37.66050, 101.42356	3556	3.0	1.00	9.644	0.246	333.18 ± 11.28	567.9 ± 28.4	07KNSTD	—	—
Gangshiqia	QS-GG-012	37.65486, 101.41586	3480	3.0	1.00	8.096	0.2446	371.43 ± 18.85	749.9 ± 54.9	07KNSTD	—	—
Gangshiqia	QS-GG-013	37.65825, 101.43286	3640	2.0	1.00	11.253	0.2446	373.75 ± 9.50	542.9 ± 21	07KNSTD	—	—
Aksaiqin glacier	AG1-1	35.39662, 80.34292	5450	0.5	1.00	—	—	—	4461.7 ± 177.3	KNSTD	25,801.3 ± 1245.9	KNSTD
Aksaiqin glacier	AG1-2	35.39650, 80.34284	5450	5.0	1.00	—	—	—	2432.8 ± 76	KNSTD	17,482.2 ± 913.4	KNSTD
Aksaiqin glacier	AG1-3	35.39938, 80.37218	5510	0.5	1.00	—	—	—	1801 ± 43.4	KNSTD	9556.4 ± 522.7	KNSTD
Aksaiqin glacier	AG1-4	35.39938, 80.37218	5510	1.0	1.00	—	—	—	4908.5 ± 118.8	KNSTD	24,213.1 ± 2076.7	KNSTD
Aksaiqin glacier	AG1-6	35.39727, 80.36554	5428	1.0	1.00	—	—	—	19,721.3 ± 585.8	KNSTD	124,199.2 ± 6767.3	KNSTD
Aksaiqin lake	LAS-1	35.25530, 79.74365	4857	1.5	1.00	—	—	—	1694.7 ± 50.5	KNSTD	9702.3 ± 635.9	KNSTD
Aksaiqin lake	LAS-1_split-a	35.26044, 79.74630	4857	1.5	1.00	—	—	—	5700 ± 155.5	KNSTD	28,731 ± 1268.7	KNSTD
Aksaiqin lake	LAS-1_split-b	35.26044, 79.74630	4857	1.5	1.00	—	—	—	21,588.4 ± 566.1	KNSTD	93,634.1 ± 4149	KNSTD
Aksaiqin lake	LAS-1_split-c	35.26044, 79.74630	4857	1.5	1.00	—	—	—	765.9 ± 28.1	KNSTD	4522.2 ± 200.3	KNSTD
Aksaiqin lake	LAS-1_split-d	35.26044, 79.74630	4857	1.5	1.00	—	—	—	2226.6 ± 68.8	KNSTD	12,958 ± 619.3	KNSTD
Aksaiqin lake	LAS-2	35.25530, 79.74365	4859	1.5	1.00	—	—	—	2389.5 ± 81.4	KNSTD	13,079.5 ± 607.6	KNSTD
Aksaiqin lake	LAS-3	35.25530, 79.74365	4863	1.5	1.00	—	—	—	1159.9 ± 77.7	KNSTD	8155.7 ± 939.2	KNSTD
Aksaiqin lake	LAS-4	35.25530, 79.74365	4875	1.5	1.00	—	—	—	2809.4 ± 86.8	KNSTD	15,970.7 ± 734.1	KNSTD
Karakax-A	KG1-5	36.44554, 77.64460	5357	1.5	1.00	—	—	—	1621.9 ± 54.2	KNSTD	8490.3 ± 375.8	KNSTD
Karakax-A	KG1-6	36.42616, 77.64395	4980	1.5	1.00	—	—	—	8070.1 ± 284.5	KNSTD	50,278.3 ± 2357.6	KNSTD
Karakax-A	KG1-7	36.42616, 77.64395	4980	2.0	1.00	—	—	—	7013.7 ± 205.2	KNSTD	42,906.5 ± 2085	KNSTD

(*Continued*)

TABLE 1. DATA FOR COSMOGENIC NUCLIDE ANALYSIS (*Continued*)

Site	Sample	Location (°N, °E)	Elevation (m asl)	Thickness (cm)	Shielding factor	Quartz* (g)	Be carrier (mg)	$^{10}Be/^{9}Be$ ($\times10^{-15}$)	^{10}Be concentration ($\times10^{3}$ atoms g^{-1} SiO_2)	^{10}Be standard†	^{26}Al concentration§ ($\times10^{3}$ atoms g^{-1} SiO_2)	^{26}Al standard#
Karakax-A	KG1-8	36.43024, 77.65266	5100	1.5	1.00	—	—	—	9584.6 ± 282.2	KNSTD	55,679.3 ± 2661.3	KNSTD
Karakax-A	KG1-9	36.43243, 77.65229	5115	1.0	1.00	—	—	—	7992.4 ± 211.6	KNSTD	49,391.9 ± 2303.8	KNSTD
Karakax-A	KG1-10	36.44317, 77.65680	5225	2.5	1.00	—	—	—	8477.7 ± 224.7	KNSTD	49,003.3 ± 2212.3	KNSTD
Karakax-A	KG1-11	36.44196, 77.65471	5223	3.0	1.00	—	—	—	2389.5 ± 81.4	KNSTD	13,079.5 ± 607.6	KNSTD
Karakax-A	KG1-12	36.44740, 77.65641	5330	3.0	1.00	—	—	—	14.6 ± 3.3	KNSTD	66.6 ± 14	KNSTD
Karakax-A	KG1-13	36.44506, 77.65725	5270	1.5	1.00	—	—	—	—	KNSTD	21,574.9 ± 989.2	KNSTD
Karakax-A	KG1-14	36.41666, 77.66410	4900	3.0	1.00	—	—	—	26,433.1 ± 768.2	KNSTD	145,706.8 ± 12,813.8	KNSTD
Karakax-A	KG1-15	36.42323, 77.67547	4940	3.0	1.00	—	—	—	9881.9 ± 341.4	KNSTD	59,997.3 ± 3134.3	KNSTD
Karakax-A	LIA-K-1	36.43898, 77.64720	5180	2.5	1.00	—	—	—	6.1 ± 26.3	KNSTD	63.7 ± 78.8	KNSTD
Karakax-A	LIA-K-2	36.44025, 77.64728	5185	1.5	1.00	—	—	—	687.6 ± 25.8	KNSTD	3934.4 ± 194.2	KNSTD
Karakax-A	LIA-K-3	36.43989, 77.64718	5195	2.0	1.00	—	—	—	1024.1 ± 46.7	KNSTD	6460 ± 305.8	KNSTD
Karakax-A	LIA-K-4	36.43898, 77.64720	5200	2.5	1.00	—	—	—	25.9 ± 4.2	KNSTD	117.2 ± 13.1	KNSTD
Karakax-B	KG2-1	36.43685, 77.68216	4900	3.5	1.00	—	—	—	7225.5 ± 273	KNSTD	46,252.1 ± 4125.3	KNSTD
Karakax-B	KG2-2	36.42821, 77.69914	4700	2.0	0.99	—	—	—	7158.5 ± 215.3	KNSTD	44,230.5 ± 3965.9	KNSTD
Karakax-B	KG2-3	36.42720, 77.70940	4585	0.5	1.00	—	—	—	7197.5 ± 199.7	KNSTD	44,813.3 ± 2864.3	KNSTD

*Density of 2.65 g cm^{-3} was used based on the quartz vein and granitic composition of the surface samples. Weight of quartz and Be carrier, and $^{10}Be/^{9}Be$ ratio are missing for some samples analyzed more than 20 yr ago.

†AMS (accelerator mass spectrometry) isotope ratios of $^{10}Be/^{9}Be$ measured using KNSTD standard were normalized to $^{10}Be/Be$ standards prepared by Nishiizumi et al. (2007) with a nominal value of $^{10}Be/Be = 2.85 \times 10^{-12}$. Samples measured using 07KNSTD were normalized to the standard NIST 4325-SRM with a $^{10}Be/Be$ value of 27.9×10^{-12} or 07KN-5-2 with a $^{10}Be/Be$ value of 8.56×10^{-12}. The isotope ratios are available in Table S1 (Supplemental Material [see text footnote 1]).

§The ^{26}Al concentrations were calculated using AMS isotope ratios of $^{26}Al/^{27}Al$ measured at the Center for Accelerator Mass Spectroscopy at the Lawrence Livermore National Laboratory, but the data for ratios were lost.

#Descriptions for the KNSTD standard are available in Nishiizumi (2004).

TABLE 2. ^{10}Be AND ^{26}Al EXPOSURE AGES REPORTED IN THIS STUDY

Site	Sample name	Location (°N, °E)	Elevation (m asl)	^{10}Be age* (ka ± ext. 1σ)	^{26}Al age* (ka ± ext. 1σ)	Sampling date (mm/dd/yy)
Kax Kurta	XCS-120a	47.46109, 89.87250	2794	16.8 ± 1.6	19.6 ± 2.1	07/09/94
Kax Kurta	XCS-120b	47.46109, 89.87250	2794	17.7 ± 1.7	16.6 ± 1.9	07/09/94
Kax Kurta	XCS-121	47.46111, 89.79944	2486	21.6 ± 2.5	22.5 ± 2.4	07/10/94
Diehanjelegou	XCS-101	43.15883, 87.44098	3080	38.6 ± 3.6	39.4 ± 3.9	06/25/94
Diehanjelegou	XCS-102	43.15901, 87.44026	3122	21.4 ± 2	20.5 ± 2.1	06/25/94
Diehanjelegou	XCS-103	43.15751, 87.45024	3014	55.7 ± 5.2	51.2 ± 5.1	06/27/94
Diehanjelegou	XCS-104	43.15690, 87.44908	3025	30.0 ± 3.1	43.3 ± 4.5	06/27/94
Diehanjelegou	XCS-105	43.15690, 87.44908	3025	42.0 ± 4.2	44.4 ± 4.6	06/27/94
Diehanjelegou	XCS-106	43.15690, 87.44908	3025	23.8 ± 2.2	25.0 ± 2.5	06/27/94
Alashanje	CS-111a	42.92695, 86.87829	3267	84.0 ± 7.7	87.7 ± 8.9	07/01/94
Alashanje	CS-111b	42.92695, 86.87829	3267	51.3 ± 4.7	55.0 ± 5.6	07/01/94
Alashanje	CS-112	43.02119, 86.97594	3658	18.7 ± 2.1	20.2 ± 2.5	07/02/94
Daxigou	CS-10	43.11882, 86.92159	3181	15.4 ± 1.5	—	09/11/92
Daxigou	CS-11b	43.11040, 86.94462	3021	23.2 ± 2.2	—	09/11/92
Daxigou	CS-12a	43.11040, 86.94462	2992	19.4 ± 2	20.4 ± 2.2	09/11/92
Daxigou	CS-5	43.11586, 86.82338	3718	0.4 ± 0.2	—	09/11/92
Daxigou	CS-6	43.11586, 86.82338	3718	1.5 ± 0.3	—	09/11/92
Daxigou	CS-7b	43.11556, 86.84138	3592	16.7 ± 1.6	15.4 ± 1.7	09/11/92
Daxigou	CS-8	43.11951, 86.92004	3417	18.6 ± 1.8	17.3 ± 1.8	09/11/92
Muzart	CS-28	41.78571, 80.90608	1978	15.4 ± 1.8	18.2 ± 1.6	09/22/92
Muzart	CS-30	41.79149, 80.90501	2011	16.6 ± 1.7	14.7 ± 1.7	09/22/92
Muzart	CS-32	41.77471, 80.95658	1889	18.2 ± 1.8	—	09/22/92
Muzart	CS-33	41.77288, 80.95874	1874	25.2 ± 4.6	—	09/22/92
Tailan	CS-14	41.60214, 80.48376	1677	6.3 ± 0.9	4.9 ± 0.6	09/16/92
Tailan	CS-20	41.65480, 80.45959	2053	12.8 ± 1.4	11.1 ± 1.2	09/18/92
Tailan	CS-24	41.63056, 80.46984	1879	8.8 ± 1.6	10.3 ± 1.3	09/19/92
Tailan	CS-27a	41.54257, 80.48545	1565	6.6 ± 0.9	4.1 ± 0.6	09/20/92
Barskoon	BS-001A	41.88323, 77.70568	3822	0.3 ± 0.1	—	06/10/11
Barskoon	BS-002A	41.88323, 77.70568	3822	0.5 ± 0.1	—	06/10/11
Barskoon	BS-002B	41.88323, 77.70568	3822	0.3 ± 0.1	—	06/10/11
Barskoon	BS-004A	41.88288, 77.70610	3831	1.2 ± 0.2	—	06/10/11
Barskoon	BS-007A	41.87017, 77.73407	3791	15.7 ± 1.4	—	06/10/11
Barskoon	BS-007B	41.87017, 77.73407	3791	15.6 ± 1.4	—	06/10/11
Barskoon	BS-007C	41.86975, 77.73563	3805	18.5 ± 1.8	—	06/10/11
Barskoon	BS-007D	41.86975, 77.73563	3805	12.2 ± 1.5	—	06/10/11
Suek	SO-CS-001	41.70825, 77.80538	3432	19.9 ± 1.9	—	06/09/11
Suek	SO-CS-002A	41.70142, 77.81050	3402	14.0 ± 1.3	—	06/09/11
Suek	SO-CS-002B	41.70142, 77.81050	3402	21.7 ± 2.1	—	06/09/11
Gulbel	GP-001	42.03892, 77.12420	2803	15.4 ± 1.9	—	06/10/11
Gulbel	GP-002A	42.01147, 77.19960	3254	17.6 ± 1.6	—	06/10/11
Gulbel	GP-002C	42.01070, 77.19833	3258	15.9 ± 1.5	—	06/10/11
Gulbel	GP-002D	42.01238, 77.20202	3208	17.0 ± 1.5	—	06/10/11
Gulbel	GP-003A	42.01432, 77.19927	3265	17.5 ± 1.7	—	06/10/11
Gulbel	GP-003B	42.01432, 77.19927	3265	16.4 ± 1.7	—	06/10/11
Gulbel	GP-003C	42.01447, 77.19822	3252	18.1 ± 1.6	—	06/10/11
Gulbel	GP-004A	42.03813, 77.14208	3001	13.2 ± 1.3	—	06/10/11
Gulbel	GP-004B	42.03813, 77.14208	3001	49.4 ± 4.9	—	06/10/11
Gulbel	GP-005	42.03828, 77.12057	2781	22.0 ± 2.0	—	06/10/11
Gulbel	GP-006	42.03822, 77.12402	2798	21.7 ± 2.0	—	06/10/11
Choktal	CR-001A	42.70139, 76.70089	3197	22.1 ± 2.0	—	06/11/11
Choktal	CR-001B	42.70139, 76.70089	3197	23.5 ± 2.2	—	06/11/11
Choktal	CR-001C	42.70139, 76.70089	3197	21.0 ± 1.9	—	06/11/11
Choktal	CR-002A	42.74965, 76.69540	3574	0.3 ± 0.1	—	06/12/11
Choktal	CR-002D	42.75083, 76.69513	3588	0.3 ± 0.1	—	06/12/11
Choktal	CR-002E	42.75083, 76.69513	3588	0.3 ± 0.1	—	06/12/11
Choktal	CR-003A	42.74775, 76.69392	3535	15.2 ± 1.4	—	06/12/11
Choktal	CR-003C	42.74775, 76.69392	3535	15.1 ± 1.4	—	06/12/11
Choktal	CR-003D	42.74707, 76.69433	3534	15.8 ± 1.4	—	06/12/11
Altyn Tagh	CAT-02C	39.31450, 93.74186	4401	1.4 ± 0.2	—	09/23/11

(*Continued*)

TABLE 2. ^{10}Be AND ^{26}Al EXPOSURE AGES REPORTED IN THIS STUDY (*Continued*)

Site	Sample name	Location (°N, °E)	Elevation (m asl)	^{10}Be age* (ka ± ext. 1σ)	^{26}Al age* (ka ± ext. 1σ)	Sampling date (mm/dd/yy)
Dumda	CH-DU-01	37.85994, 96.28808	4039	125.4 ± 11.4	—	09/20/11
Dumda	CH-DU-02	37.85203, 96.28636	4036	158.6 ± 14.7	—	09/20/11
Dumda	CH-DU-03	37.86278, 96.28833	4056	137.6 ± 12.8	—	09/20/11
Gangshiqia	QS-GG-001	37.6936, 101.45208	4085	11.3 ± 1.1	—	09/16/11
Gangshiqia	QS-GG-002	37.6936, 101.45208	4085	13.5 ± 1.2	—	09/16/11
Gangshiqia	QS-GG-003	37.6942, 101.45319	4101	14.5 ± 1.3	—	09/16/11
Gangshiqia	QS-GG-004	37.6942, 101.45319	4101	14.9 ± 1.3	—	09/16/11
Gangshiqia	QS-GG-005	37.6942, 101.45319	4120	3.8 ± 0.4	—	09/16/11
Gangshiqia	QS-GG-006	37.6944, 101.45417	4120	3.1 ± 0.3	—	09/16/11
Gangshiqia	QS-GG-007	37.6911, 101.45194	4041	12.2 ± 1.1	—	09/16/11
Gangshiqia	QS-GG-008	37.6634, 101.42669	3615	18.7 ± 1.9	—	09/17/11
Gangshiqia	QS-GG-009	37.6634, 101.42669	3615	17.7 ± 1.6	—	09/17/11
Gangshiqia	QS-GG-010	37.6605, 101.42356	3556	14.9 ± 1.6	—	09/17/11
Gangshiqia	QS-GG-011	37.6605, 101.42356	3556	13.1 ± 1.3	—	09/17/11
Gangshiqia	QS-GG-012	37.6549, 101.41586	3480	18.0 ± 2.0	—	09/17/11
Gangshiqia	QS-GG-013	37.6583, 101.43286	3640	11.8 ± 1.1	—	09/17/11
Aksaiqin glacier	AG1-1	35.39662, 80.34292	5450	39.7 ± 3.8	37.9 ± 3.8	04/07/95
Aksaiqin glacier	AG1-2	35.39650, 80.34284	5450	22.4 ± 2.1	26.5 ± 2.7	04/07/95
Aksaiqin glacier	AG1-3	35.39938, 80.37218	5510	15.5 ± 1.4	13.5 ± 1.4	04/07/95
Aksaiqin glacier	AG1-4	35.39938, 80.37218	5510	42.8 ± 3.8	34.8 ± 4.3	04/07/95
Aksaiqin glacier	AG1-6	35.39727, 80.36554	5428	184.5 ± 17.5	200.1 ± 22.4	04/07/95
Aksaiqin Lake	LAS-1	35.25530, 79.74365	4857	19.8 ± 1.8	18.6 ± 2	08/01/95
Aksaiqin Lake	LAS-1_split-a	35.26044, 79.74630	4857	67.4 ± 6.2	56.2 ± 5.6	08/01/95
Aksaiqin Lake	LAS-1_split-b	35.26044, 79.74630	4857	268.4 ± 25.7	196.0 ± 20.8	08/01/95
Aksaiqin Lake	LAS-1_split-c	35.26044, 79.74630	4857	8.9 ± 0.8	8.7 ± 0.8	08/01/95
Aksaiqin Lake	LAS-1_split-d	35.26044, 79.74630	4857	26.1 ± 2.4	25.2 ± 2.5	08/01/95
Aksaiqin Lake	LAS-2	35.25530, 79.74365	4859	28 ± 2.6	25.2 ± 2.5	08/01/95
Aksaiqin Lake	LAS-3	35.25530, 79.74365	4863	13.5 ± 1.5	15.6 ± 2.3	08/01/95
Aksaiqin Lake	LAS-4	35.25530, 79.74365	4875	32.7 ± 3	30.6 ± 3.0	08/01/95
Karakax-A	KG1-5	36.44554, 77.64460	5357	14.4 ± 1.3	12.4 ± 1.2	04/07/95
Karakax-A	KG1-6	36.42616, 77.64395	4980	86.3 ± 8.2	90 ± 9.2	04/07/95
Karakax-A	KG1-7	36.42616, 77.64395	4980	75.1 ± 6.9	76.6 ± 7.8	04/07/95
Karakax-A	KG1-8	36.43024, 77.65266	5100	97.4 ± 9	94.6 ± 9.7	04/07/95
Karakax-A	KG1-9	36.43243, 77.65229	5115	80.0 ± 7.3	82.5 ± 8.4	04/07/95
Karakax-A	KG1-10	36.44317, 77.65680	5225	81.8 ± 7.5	78.8 ± 7.9	04/07/95
Karakax-A	KG1-11	36.44196, 77.65471	5223	22.8 ± 2.1	20.5 ± 2.0	04/07/95
Karakax-A	KG1-12	36.44740, 77.65641	5330	0.1 ± 0	0.1 ± 0.05	04/07/95
Karakax-A	KG1-13	36.44506, 77.65725	5270	—	33 ± 3.3	04/07/95
Karakax-A	KG1-14	36.41666, 77.66410	4900	314.1 ± 30.7	303.3 ± 43.3	04/07/95
Karakax-A	KG1-15	36.42323, 77.67547	4940	109.6 ± 10.4	111.9 ± 11.8	04/07/95
Karakax-A	LIA-K-1	36.43898, 77.64720	5180	0.1 ± 0.3	0.1 ± 0.1	04/07/95
Karakax-A	LIA-K-2	36.44025, 77.64728	5185	6.6 ± 0.6	6.2 ± 0.6	04/07/95
Karakax-A	LIA-K-3	36.43989, 77.64718	5195	9.8 ± 1.0	10.1 ± 1	04/07/95
Karakax-A	LIA-K-4	36.43898, 77.64720	5200	0.3 ± 0.1	0.2 ± 0	04/07/95
Karakax-B	KG2-1	36.43685, 77.68216	4900	81.4 ± 7.8	87.2 ± 11.2	04/07/95
Karakax-B	KG2-2	36.42821, 77.69914	4700	88.5 ± 8.2	91.5 ± 11.9	04/07/95
Karakax-B	KG2-3	36.42720, 77.70940	4585	92.0 ± 8.5	95.9 ± 10.7	04/07/95

*The ^{10}Be and ^{26}Al exposure ages were calculated using CRONUS-Earth (Balco et al., 2008), version 2.3, with ^{10}Be and ^{26}Al production rates by Borchers et al. (2016). The density of the samples was assumed to be 2.65 g cm^{-3}. No erosion was applied in age calculations. We used the exposure ages based on the constant production rate model with the spallation scaling scheme of Lal (1991) and Stone (2000). Propagated 1σ "external" uncertainty in the model age includes "internal" uncertainties introduced in the calculation of the ^{10}Be and ^{26}Al concentrations, in addition to a 5.5% uncertainty in the production rate of ^{10}Be and a 1% uncertainty in the ^{10}Be decay constant.

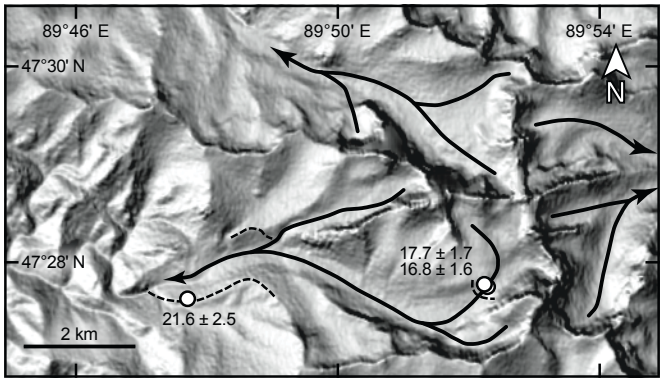

Figure 3. ^{10}Be samples in Kax Kurta valley, Altai range. Circles indicate the locations of ^{10}Be and ^{26}Al samples. Black arrows indicate the directions of paleo-outlet glaciers. Dashed lines indicate the moraine crests. The background image shaded relief image was constructed using Shuttle Radar Topography Mission (SRTM) 30-m-resolution digital elevation model (DEM) data (1 arc-second global data; U.S. Geological Survey, 2018b).

moraine that corresponds to a *THAR* ELA of ~3620 m asl. The valley contains two cirques now narrowly separated by a ridge, but the dated paleoglacier filled both cirques, overtopping the ridges. The highest modern glacier in the cirque has *THAR* ELA of ~3870 m asl (annual *ppt* ~250 m and summer T_{air} = 7.4 ± 0.9 °C at the ELA).

East Tian Shan, Alashanje

We sampled two boulders from an outermost right-lateral moraine in the lower part of the Alashanje valley (Fig. 4C), which gave a mean ^{10}Be age of 67.7 ± 24.8 ka. Li et al. (2014) collected three samples on the upper part of the moraine to derive a mean ^{10}Be age of 76.1 ± 11.2 ka after one outlier was rejected. On the other side of the river, an end moraine sits at a similar altitude to the lower portion of the right-lateral moraine, and Li et al. (2014) dated it to a mean ^{10}Be age of 46.8 ± 12.3 ka (n = 7, one outlier). This end moraine corresponds to a *THAR* ELA of ~3770 m asl. However, the evidence for the maximum paleoglacier extent in this valley, the eroded hummocky till overlying the local fan, can be found further down the valley ~340 m in altitude below the dated moraines. The glaciated surface was not dated, and the lowest altitude of this hummocky terrain corresponds to a *THAR* ELA of ~3710 m asl. About 15 km up valley and ~850 m above this moraine from the maximum paleoglacier extent, two closely located end moraines were dated to 28.8 ± 6.6 and 25.8 ± 5.2 ka (Li et al., 2014). The highest of the dated moraines in the valley, 17.5 ± 5.8 ka (Li et al., 2014), was found only ~210 m below and ~2 km away from the modern glacier tongue. The peaks around this site are ~400 m higher than the peaks around the Diehanjelegou valley, and the higher altitude of the Alashanje site is reflected in the colder summer T_{air} of ~3.4 ± 0.7 °C, although they are in close proximity and receive the same annual *ppt* of ~250 m.

East Tian Shan, Daxigou

The paleoglaciers in the trunk Daxigou valley were fed by smaller glaciers sourced from 13 separate cirques, mostly oriented northward (Fig. 4D). The valley itself trends E, unlike the northward-facing Diehanjelegou and south-facing Alashanje valleys. Despite the large number of tributary valleys contributing glacier ice, the U-shaped Daxigou valley extends for only ~16 km until it becomes a V-shaped valley with no evidence of glaciation. The rough outline of this paleoglacier, the largest in Daxigou, can be traced from the trimlines found especially on the southern side of the valley. The *THAR* ELA for this paleoglacier was ~3570 m asl, the value for the local LGM. Approximately 4 km up valley from the inferred end of the local LGM glacier, Li et al. (2011) collected two boulders from a left-lateral moraine and ^{10}Be dated them to ca. 21 and 18 ka. We collected two additional boulders from the same moraine, ^{10}Be-dated to ca. 23 and 19 ka, and the total of the four boulders gave a mean ^{10}Be age of 19.3 ± 3.6 ka (n = 4, one outlier). This standstill within the global LGM corresponds to an estimated *THAR* ELA of ~3670 m asl, ~120 m higher than for the local LGM. About 2 km up valley, we sampled two boulders from a previously studied lateral moraine (Li et al., 2014), and the total of six boulders gave a mean ^{10}Be age of 17.4 ± 4.2 ka. Another moraine nearby was ^{10}Be-dated to 17.7 ± 2.5 ka (n = 3, one outlier; Kong et al., 2009). This location was on a broad flat area only ~220 m below the modern glaciers' termini. There, the ^{10}Be age of a boulder we collected from an end moraine was added to four ^{10}Be ages previously reported by Kong et al. (2009) to give a mean ^{10}Be age of 19.6 ± 5.4 ka (after one outlier was deleted). Only 300 m away, Li et al. (2011) dated another moraine to obtain a mean ^{10}Be age of 17.3 ± 2.3 ka (n = 2). These moraines correspond to a *THAR* ELA of ~3900 m asl, which is only ~100 m below the estimated modern ELA. These ages and the estimated paleo-ELAs suggest that the paleoglacier in Daxigou receded dramatically at the end of the global LGM, from ~80% to ~40% of the local LGM ΔELA_{norm} within ~2000 yr. The youngest moraine in the valley, a nearby unbreached end moraine, was located ~100 m below the modern glacier terminus, which was dated to 0.3 ± 0.3 ka (n = 8, one outlier; Li et al., 2014; this study). The *THAR* ELA for the modern glacier, ~4000 m asl, represents a ΔELA_{norm} of ~25% in Daxigou.

West Tian Shan, Muzart

The western section of the Tian Shan range extends ~1200 km from the west in Kyrgyzstan to the east in China (Fig. 1). The large alluvial fan emanating from Muzart valley is overlain by a series of at least 14 end moraines. We sampled two boulders from the outermost moraine, which gave a mean ^{10}Be age of 21.7 ± 7.0 ka (*THAR* ELA 4490 m asl; Fig. 5). Up valley ~4.5 km from this lowest moraine, we sampled two more boulders with a mean ^{10}Be age of 16.0 ± 2.6 ka (*THAR* ELA ~4520 m asl). The paleoglaciers that deposited the dated piedmont moraines were sourced from today's glaciated cirques with various orientations. Because

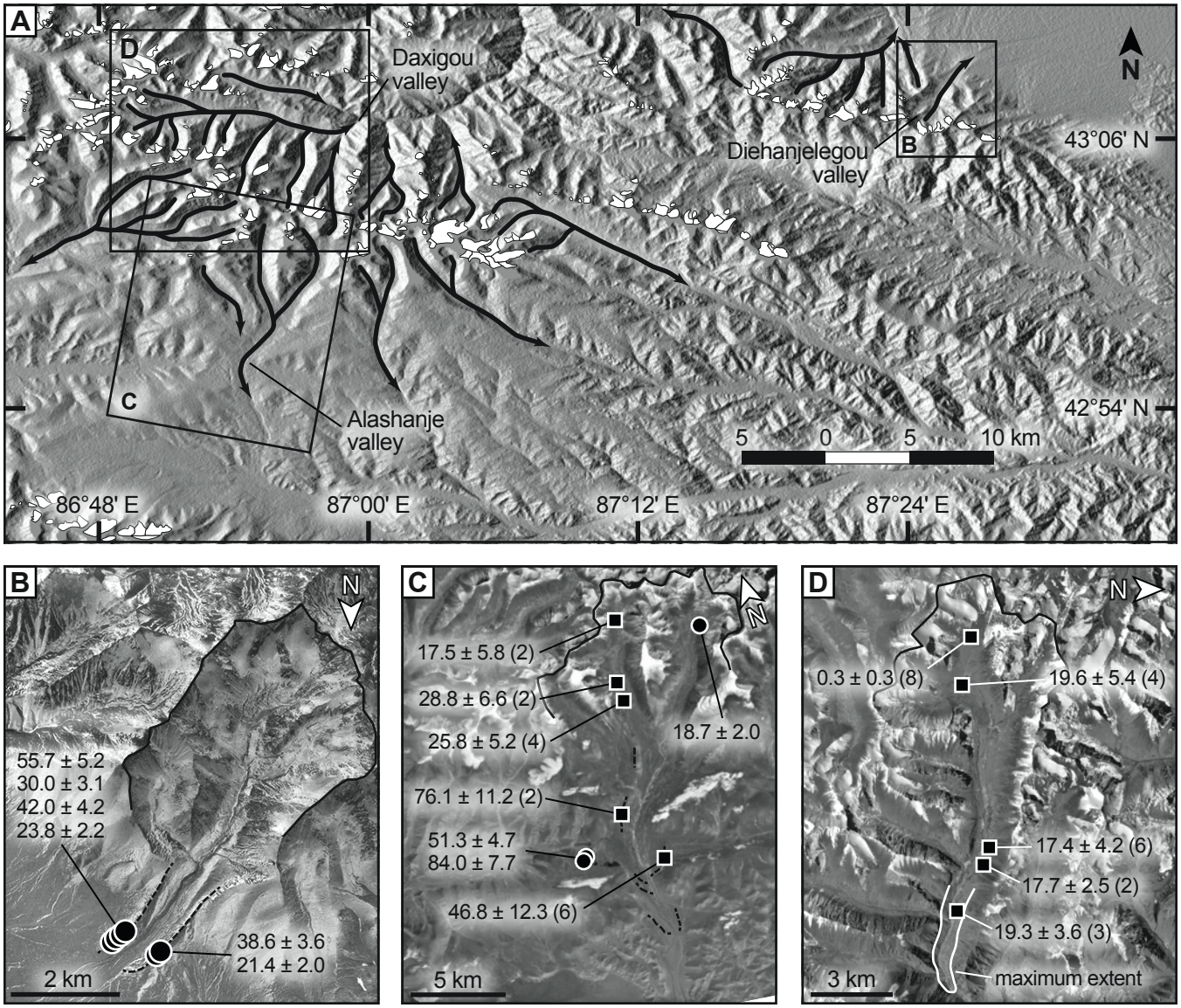

Figure 4. Study sites in the East Tian Shan. (A) Map showing the directions of major paleo-outlet glaciers (black arrows) and the extent of modern glaciers (white polygons). The background shaded relief image was constructed using Advanced Spaceborne Thermal Emission and Reflection Radiometer (ASTER) Global Digital Elevation Model (GDEM) V2 (NASA and METI, 2017); (B) Diehanjelegou valley (background Google Earth image); (C) Alashanje valley (ASTER image; NASA and METI, 2001); (D) Daxigou valley (ASTER image; NASA and METI, 2001). The circles indicate individual ^{10}Be and ^{26}Al samples. The squares represent mean ^{10}Be ages after rejecting outliers, in ka ± 1σ total uncertainty (number of samples in parentheses), calculated using data reported in this study, Kong et al. (2009), Li et al. (2011), and Li et al. (2014). The dashed lines are moraine crests. The moraines ridges were too small to be visible on Figure 4D. The maximum glacier extent in Figure 4D was inferred from trimlines. The thin black lines delineate the arêtes. See text for details of those individual samples that were included in the calculations of the mean ^{10}Be ages. The extent of modern glaciers was from RGI 6.0 (RGI Consortium, 2017).

of this complexity, the absolute *THAR* ELA values for the two piedmont moraines may not be readily comparable to the *THAR* ELAs estimated for smaller glaciers with simple geometry. However, the ΔELA_{norm} values within Muzart valley may provide a better comparison of relative glacial extents and their timing in comparison to other glaciers in central Asia. The modern glaciers were estimated to have *THAR* ELAs of ~4820 m asl (summer T_{air} of 0.1 ± 0.7 °C; annual *ppt* ~150 mm), which represent a ΔELA_{norm} of ~80%.

West Tian Shan, Tailan

Approximately 40 km to the west of the Muzart piedmont, a large alluvial fan emanates from the mouth of Tailan valley (Fig.

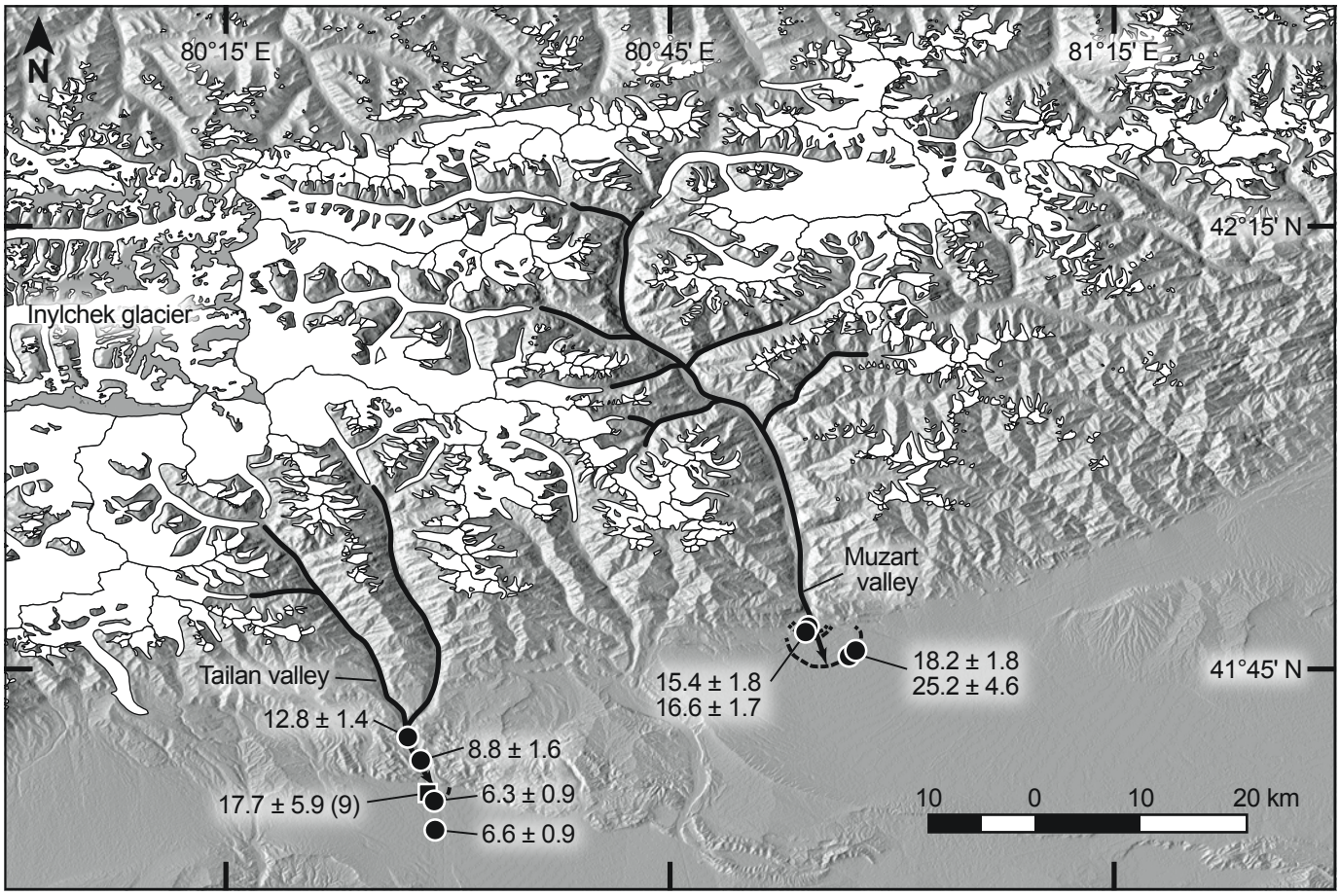

Figure 5. The Muzart and Tailan sites in the West Tian Shan. The white polygons indicate the extent of modern glaciers (RGI 6.0; RGI Consortium, 2017). The black arrows indicate direction of outlet glaciers from the ice field. The dashed lines indicate moraine crests. Circles indicate the individual ^{10}Be ages, in ka ± 1σ external uncertainty, reported in this study. The square is a mean ^{10}Be age, ka ± 1σ total uncertainty (number of samples in the mean), calculated using data from Hubert-Ferrari et al. (2005). The background shaded relief was constructed using Shuttle Radar Topography Mission (SRTM) digital elevation model (DEM) data (GTOPO30; U.S. Geological Survey, 2017).

5). We collected a boulder from the fan, which gave a ^{10}Be age of 6.6 ± 0.9 ka. Close to the mouth of the valley, there are at least seven sets of moraines. Hubert-Ferrari et al. (2005) collected 10 glacial boulders that gave a mean ^{10}Be age of 17.7 ± 5.9 ka (after one outlier was removed), from a moraine that corresponded to a *THAR* ELA of 3970 m asl. A sample from a boulder sitting on the isolated remnant of the lowest moraine yielded a ^{10}Be age of 6.3 ± 0.9 ka, which we suspect suffered from rolling or burial after deposition. We sampled a boulder ~1.5 km upstream from a moraine ridge and obtained a ^{10}Be age of 8.8 ± 1.6 ka, which is too young, probably due to burial or disturbance after deposition. About 6 km upstream from the lowest moraine, a boulder sitting on a moraine ridge yielded a ^{10}Be age of 12.8 ± 1.4 ka. This age is stratigraphically consistent with the ca. 18 ka moraine, but we cannot rely on a single age of ca. 13 ka and did not consider it for ELA analysis. Although the ca. 18 ka moraine was not from the largest paleoglacier, and because the topographic gradient is low (~25 m km^{-1}), there is little difference (~35 m) between the ELAs estimated from the ca. 18 ka moraine and the lowest moraines. The modern ELA was estimated to be ~4560 m asl (ΔELA_{norm} of ~60%) with summer T_{air} of 5.3 ± 0.7 °C and annual *ppt* of ~150 mm.

The difference between the estimated summer T_{air} at the modern ELAs for Muzart and Tailan is ~5 °C, but the difference between their modern ELAs is ~250 m. Accounting for the same lapse rate estimated for these sites, the 250 m ELA difference would correspond to a T_{air} difference of only ~2 °C. There are two reasons for this discrepancy: (1) The threshold *THAR* value for the modern glacier in the Muzart valley was set slightly too high; and/or (2) the altitude of the grid cell in the T_{air} data (Fan and van den Dool, 2008) for Tailan was set ~750 m higher than for Muzart. Nevertheless, the 250 m ELA difference for these neighboring glaciers is reasonable within the accuracy of the *THAR* method despite the complications due to different cirque orientations and the heavy cover of debris.

The Inylchek glacier (Fig. 5) flows to the west, and its cirques share the ~7400–6800 m asl high peaks with the neighboring

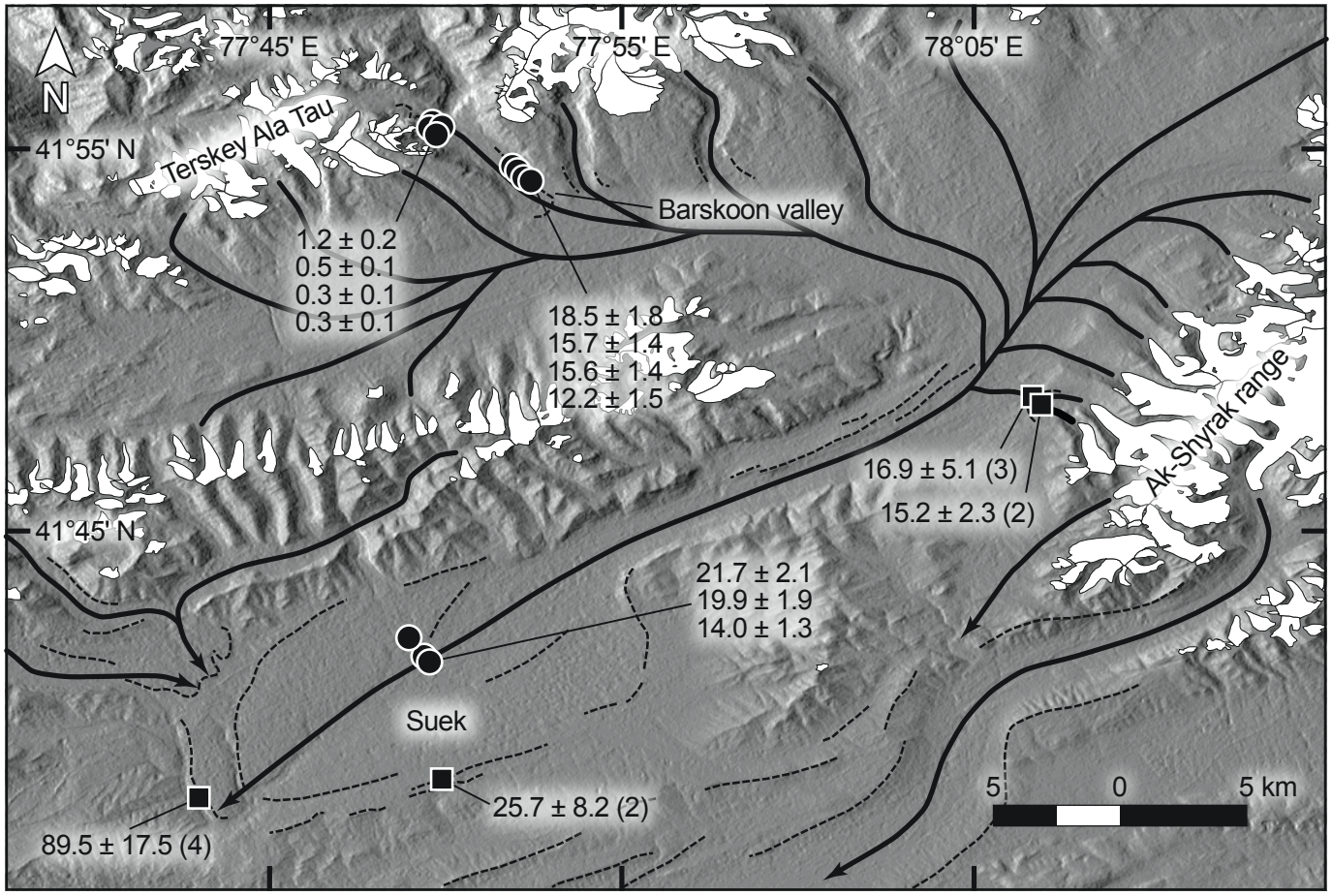

Figure 6. The Barskoon and Suek study sites in the West Tian Shan. The black arrows indicate the flow directions of paleo-outlet glaciers sourced from ice fields in Terskey Ala Tau and Ak-Shyrak ranges. The dashed lines indicate moraine crests. The circles indicate the individual ^{10}Be ages, ka ± 1σ external uncertainty, reported in this study. The squares indicate mean ^{10}Be ages, ka ± 1σ total uncertainty (number of samples in the mean), calculated using data from Blomdin et al. (2016). The extent of modern glaciers (white polygons) is from RGI 6.0 (RGI Consortium, 2017). The background shaded relief was constructed using Advanced Spaceborne Thermal Emission and Reflection Radiometer (ASTER) Global Digital Elevation Model (GDEM) V2 (NASA and METI, 2017).

Muzart and Tailan cirques. Lifton et al. (2014) found remnants of ca. 150 ka moraines (n = 2 ^{10}Be; *THAR* ELA ~4200 m asl) ~7 km downstream from a ca. 16 ka moraine (n = 2 ^{10}Be; *THAR* ELA ~4220 m asl). The ELA estimates and the ^{10}Be ages from Muzart, Tailan, and Inylchek suggest that the local LGM in this part of West Tian Shan did not occur during MIS 2 and that the global LGM glaciers were no larger than the older advances.

West Tian Shan, Barskoon and Suek

About 200 km west of Inylchek glacier, the altitude drops rapidly by ~2000 m, where the north-facing modern glaciers around the Barskoon and Suek valleys (Fig. 6) sit within their cirques. We sampled three boulders in the middle of the large moraine complex incised by the Suek river, which gave a mean ^{10}Be age of 20.8 ± 3.0 ka. Blomdin et al. (2016) sampled boulders from the outermost margins of the moraine complex that gave a mean ^{10}Be age of 25.7 ± 8.2 (n = 2) and 89.5 ± 17.5 ka (n = 5; one outlier rejection). The *THAR* ELAs for the Suek moraine complex range from 3880 to 3810 m asl. The local LGM during MIS 5 inferred from the Suek moraine complex and similar extent of glaciers during MIS 2 are consistent with the spatial and temporal pattern of glacial extents in the other sites in the West Tian Shan (Fig. 6).

The paleoglaciers that deposited the Suek moraines were sourced from two separate ice fields, one over the Terskey Ala Tau range in the north and the other over the Ak-Shyrak range in the south (Fig. 6). Near Barskoon pass, in Terskey Ala Tau, we sampled four boulders from the left-lateral moraine of a paleoglacier that once contributed to the Suek paleoglaciers. These gave a mean ^{10}Be age of 16.6 ± 3.1 ka (one outlier). From this moraine, we estimated a *THAR* ELA of ~4030 m asl, which was ~40% of the ΔELA_{norm} for local and global LGM ELAs estimated from the Suek moraines themselves. About 3 km up valley, we

sampled three boulders from an end moraine located ~500 m from the modern glacier, to obtain a mean ^{10}Be age of 0.4 ± 0.2 ka. The *THAR* ELA for this Holocene moraine, 4020 m asl, was only ~30 m lower than the modern *THAR* ELA (summer T_{air} = 2.4 ± 1.3 °C; annual *ppt* ~250 mm).

Blomdin et al. (2016) collected boulders from two end moraines sitting close to a modern glacier in the Ak-Shyrak range (Fig. 6), one of the southern sources for the Suek paleoglaciers. The moraines were dated to 16.9 ± 5.1 ka (n = 4, one outlier) and 15.2 ± 2.3 ka (n = 3, one outlier), corresponding to similar *THAR* ELAs of ~4100 m asl (~50 m lower than the local modern ELA). The timing and the spatial extents of these late global LGM moraines are consistent and suggest that the Suek paleoglaciers receded rather rapidly; within ~9000 yr, the glaciers retreated from their near-maxima (ELA increase of ~200–150 m, or length reduction of ~60–40 km) to very close proximity to the modern glaciers.

West Tian Shan, Gulbel

In the Terskey Ala Tau range, ~40 km NW of the Barskoon Pass, we sampled a set of lateral and end moraines in Korumdy river valley, near Gulbel pass (Fig. 7). There, paleoglaciers were sourced from four now-separated cirques, and during MIS 3 the paleoglaciers flowed both westward and also eastward over Gulbel pass (Koppes et al., 2008). More recently, the paleoglacier flowed only westward and did not overtop Gulbel pass. We sampled three boulders from the right-lateral moraines west of Gulbel pass, obtaining a mean ^{10}Be age of 21.9 ± 2.8 ka (after one outlier was removed). This lateral moraine can be traced to an end moraine that corresponds to a *THAR* ELA of ~3890 m asl. Near this sampling site, one boulder from the outermost moraine crest was dated to ca. 97 ka (Koppes et al., 2008). Approximately 9 km up valley, another right-lateral moraine was ^{10}Be-dated to 17.3 ± 3.0 ka (n = 3; *THAR* ELA ~3790 m asl). About 30 m below this lateral moraine, we found a remnant of an end moraine, which was ^{10}Be-dated to 16.8 ± 2.8 ka (n = 3; *THAR* ELA ~3870 m asl). The modern ELA was estimated to be ~4000 m asl (summer T_{air} = –2.2 ± 1.2 °C; annual *ppt* ~320 mm), corresponding to ~40% ΔELA_{norm}.

West Tian Shan, Choktal

The Zalisky Ala Tau range, at the border between Kyrgyzstan and Kazakhstan, marks the northernmost extent of West Tian Shan (Fig. 8). We sampled from the moraines in Choktal valley that were deposited by paleoglaciers sourced from six now-separated cirques facing south. The lowest moraines in the valley were not dated (*THAR* ELA ~3680 m asl). About 7 km up valley, three samples from the left-lateral moraine gave a mean ^{10}Be age of 22.2 ± 3.7 ka (*THAR* ELA ~3720 m asl, ~90% ΔELA_{norm}). Near one of the modern glaciers, there were two end moraines in close

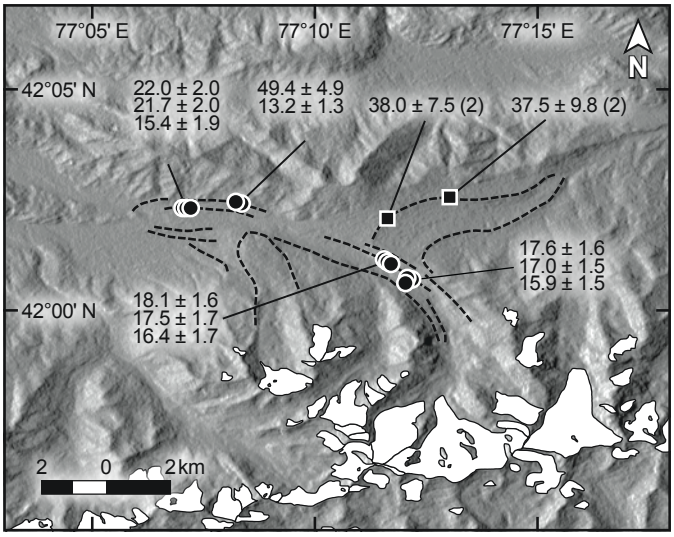

Figure 7. The Gulbel study site in the West Tian Shan. The dashed lines indicate moraine crests. The circles indicate the individual ^{10}Be ages, ka ± 1σ external uncertainty, reported in this study. The squares indicate mean ^{10}Be ages, ka ± 1σ total uncertainty (number of samples in the mean), calculated using data from Koppes et al. (2008). The extent of modern glaciers (white polygons) is from RGI 6.0 (RGI Consortium, 2017). The background shaded relief was constructed using Advanced Spaceborne Thermal Emission and Reflection Radiometer (ASTER) Global Digital Elevation Model (GDEM) V2 (NASA and METI, 2017).

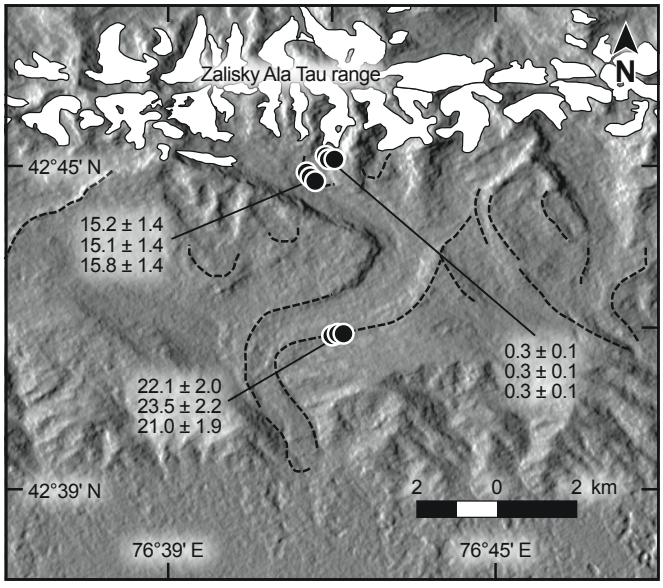

Figure 8. The Choktal study site in the West Tian Shan. The dashed lines indicate moraine crests. The circles indicate the individual ^{10}Be ages, ka ± 1σ external uncertainty, reported in this study. The extent of modern glaciers (white polygons) is from RGI 6.0 (RGI Consortium, 2017). The background shaded relief was constructed using Advanced Spaceborne Thermal Emission and Reflection Radiometer (ASTER) Global Digital Elevation Model (GDEM) V2 (NASA and METI, 2017).

proximity, which we ^{10}Be-dated to 15.4 ± 2.5 (n = 3; *THAR* ELA ~4090 m asl) and 0.3 ± 0.1 ka (n = 3; *THAR* ELA ~4110 m asl). The modern ELA was estimated to be ~4180 m asl (summer T_{air} = 7.6 ± 1.0 °C; annual *ppt* ~420 mm). The timing and the rapid recession at the end of the global LGM, and the close proximity of late Holocene moraines to the modern glacier in Choktal appear to be similar to temporal and spatial patterns of glaciation observed at the Suek and Barskoon sites.

Qilian Shan, Altyn Tagh

The glaciated part of the approximately W-E–oriented Altyn Tagh range (#6 on Fig. 1), at the northern end of the Qaidam basin, consists of two parallel mountain ridges (Fig. 9). These are ~30 km long and join the ranges of the Qilian Shan in the east. This was the most arid site among the regions considered in this study with ~65 mm annual *ppt*. The southern ridge contained granitic bedrock that would be appropriate for exposure dating. However, we were allowed to sample only from the northern part of the range, where the local rocks were too poor in quartz for ^{10}Be analysis.

The modern glacier in our studied valley is located in the north-facing cirque below the highest (5500 m asl) peak of the northern ridge (Fig. 9). We sampled a right-lateral moraine in close proximity to the modern glacier, but no sample yielded enough quartz to analyze for ^{10}Be. We sampled five schist boulders from an end moraine, only ~40 m below and ~150 m away from the modern glacier tongue, of which only one had enough quartz (from stringers) to date, and this yielded a ^{10}Be age of 1.4 ± 0.2 ka (Fig. 9B). The *THAR* ELA estimated from this moraine was ~5060 m asl. Approximately 350 m down valley from the sampled moraine, the flat cirque floor transitions into an ~60-m-wide narrow valley with steep walls. The lowest altitude of the cirque floor may place a limit on the maximum extent of the paleoglacier there. The bottom of this cirque floor yielded a *THAR* ELA of ~5030 m asl. The modern *THAR* ELA was ~5080 m asl. There was no other evidence of glaciation below the sampled moraine. We visited an adjacent north-facing valley to the west and observed a similar pattern: The end moraine was very close to the modern glacier, and we observed no evidence of a larger advance below the cirque. Summer T_{air} at the modern ELA was estimated to be 6.8 ± 1.4 °C at this site.

Qilian Shan, Dumda[2] (Dunde Ice Cap, 5325 m asl)

Approximately 270 km to the southeast of the Altyn Tagh range, the Dunde ice cap crests an approximately W-E–oriented range (Fig. 10). Thompson et al. (1989) extracted three ice cores from the Dunde ice cap and inferred from δ^{18}O ratios that the regional T_{air} was lowest during the global LGM. The modern Dunde ice cap covers only one third of the high plateau on the eastern end of the range, and the paleoglaciers sourced from the ice cap flowed to the north, south, and east, forming well-developed wide valleys (e.g., Dumda, Nariin, Zah, and Juhant

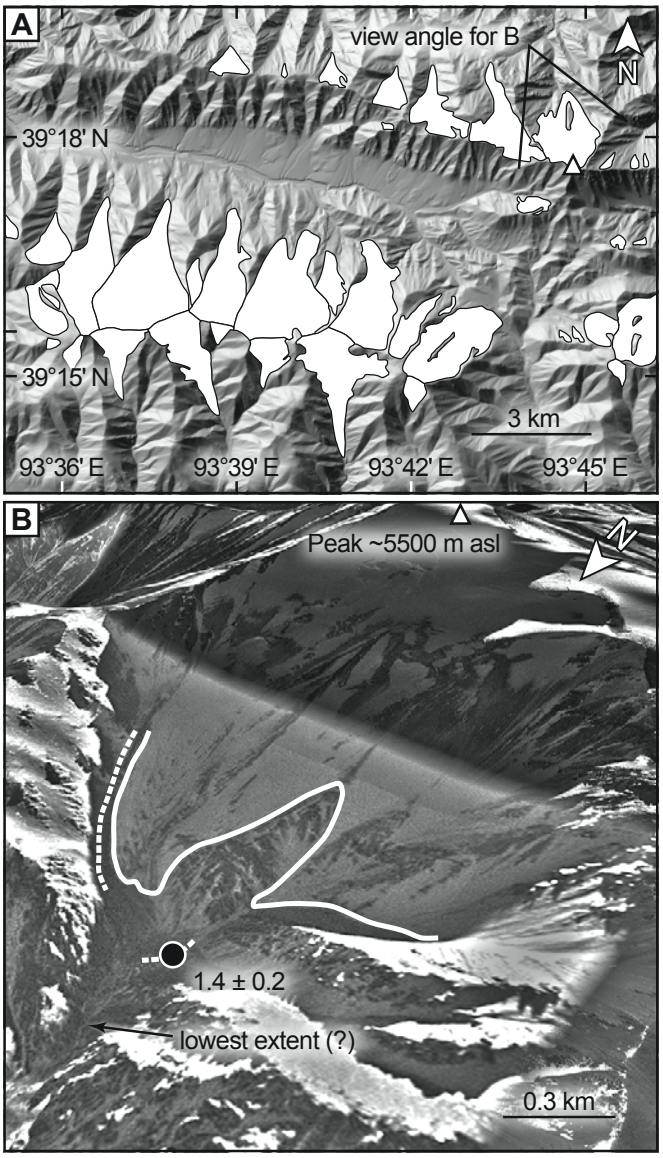

Figure 9. The Altyn Tagh study site in the northern Qilian Shan, showing (A) modern glaciers (white polygons: RGI 6.0; RGI Consortium, 2017) around the study site (background shaded relief was constructed using High Mountain Asia 8 m digital elevation models derived from along-track optical imagery, version 1; Shean, 2017); and (B) perspective view (Google Earth, DigitalGlobe) of the moraines (dashed lines) and the modern glacier tongue (white line) at the sampling site. The circle indicates the ^{10}Be age, ka ± 1σ external uncertainty, reported in this study. The lowest glacier extent (?) was inferred from the cirque floor; no evidence of glaciation was found at lower elevations.

[2]The local ethnic Mongol herders called the range "Mösön Uul," which translates from Mongolian to "icy mountain." The studied river valley is locally called "Dumda" (meaning "middle," spelling per old Mongolian script). Thompson et al. (1989) spelled the ice cap on the range "Dunde," a convention we adopt here.

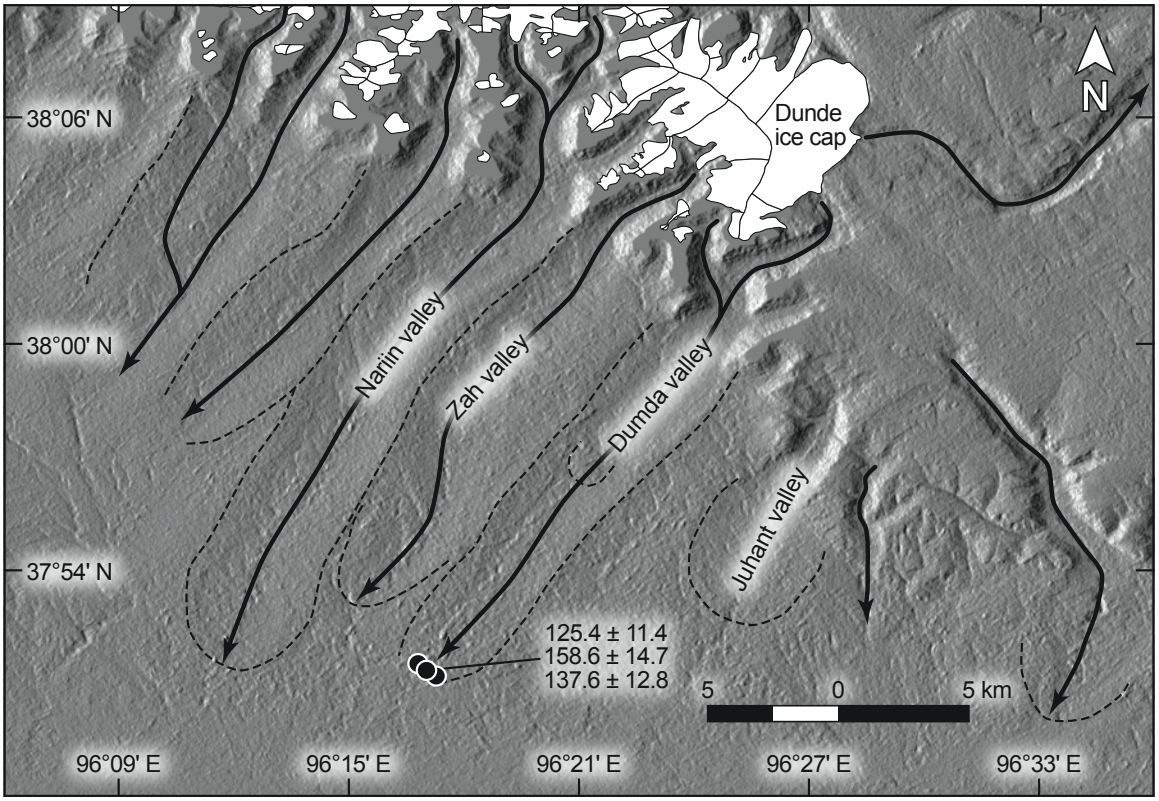

Figure 10. The Dumda study site near the Dunde ice cap in the Qilian Shan. The dashed lines indicate moraine crests. The black arrows indicate the maximum extent of the paleo-outlet glaciers sourced from the Dunde ice field. The circles indicate individual ^{10}Be ages, ka ± 1σ external uncertainty, reported in this study. The extent of modern glaciers (white polygons) is from RGI 6.0 (RGI Consortium, 2017). The background shaded relief was constructed using Advanced Spaceborne Thermal Emission and Reflection Radiometer (ASTER) Global Digital Elevation Model (GDEM) V2 (NASA and METI, 2017).

valleys in Fig. 10). We sampled from the heavily eroded end moraine marking the local LGM extent in the Dumda river valley (Figs. S18–19 [see footnote 1]). Three boulders gave a mean ^{10}Be age of 131.5 ± 19.2 ka, after rejecting one outlier identified by the normalized deviation method. However, Chauvenet's (1891) and Peirce's (Ross, 2003) criteria did not identify any outliers; without rejecting the outlier, the three ^{10}Be boulder ages would give a mean of 140.5 ± 28.1 ka. This local LGM extent corresponds to a *THAR* ELA of ~4760 m asl. About 12 km up valley from the dated moraine, another end moraine can be identified from Google Earth imagery, and this moraine corresponds to a *THAR* ELA of ~4880 m asl. The modern ELA was estimated to be ~5060 m asl (summer T_{air} = 2.4 ± 1.5 °C; annual *ppt* ~120 mm), corresponding to ~40% ΔELA_{norm}.

Qilian Shan, Gangshiqia

Located 120 km northeast of Qinghai lake, the Lenglong Ling range marks the eastern end of the Qilian Shan. The valley we studied, with a SW-facing cirque below the Gangshiqia peak (Fig. 11), has a relatively simple and straight geometry and is oriented in the SW-NE direction. The coarse-scale hummocky terrain provides evidence for stagnant ice that was left from the largest paleoglaciers in the valley. Owen et al. (2003) ^{10}Be-dated five boulders from two locations in the hummocky terrain to 13.8 ± 3.9 (n = 2) and 13.1 ± 2.4 ka (n = 3). We collected a boulder ~10 m above the location sampled by Owen et al. (2003) and ^{10}Be-dated it to 18.0 ± 2.0 ka. Close to the mouth of the valley, there are two right-lateral moraines at altitudes of ~3610 and ~3550 m asl. There, we sampled two boulders from each moraine to obtain mean ^{10}Be ages of 18.2 ± 2.6 (MELM ELA ~3710 m asl) and 14.0 ± 2.4 ka (MELM ELA ~3680 m asl), located in stratigraphic order. Approximately 7 km up valley from the piedmont, the right-lateral moraine was ^{10}Be-dated to 11.7 ± 4.9 ka (n = 6, one outlier), corresponding to a MELM ELA of ~4320 m asl. The *THAR* ELA for the modern glacier was ~4770 m asl (summer T_{air} = −1.9 ± 1.1 °C; annual *ppt* ~210 mm) at ~20% ΔELA_{norm}.

West Kunlun, Aksaiqin

Located at the southwestern end of the Tarim basin, the western Kunlun range stretches ~680 km in a NW-SE direction

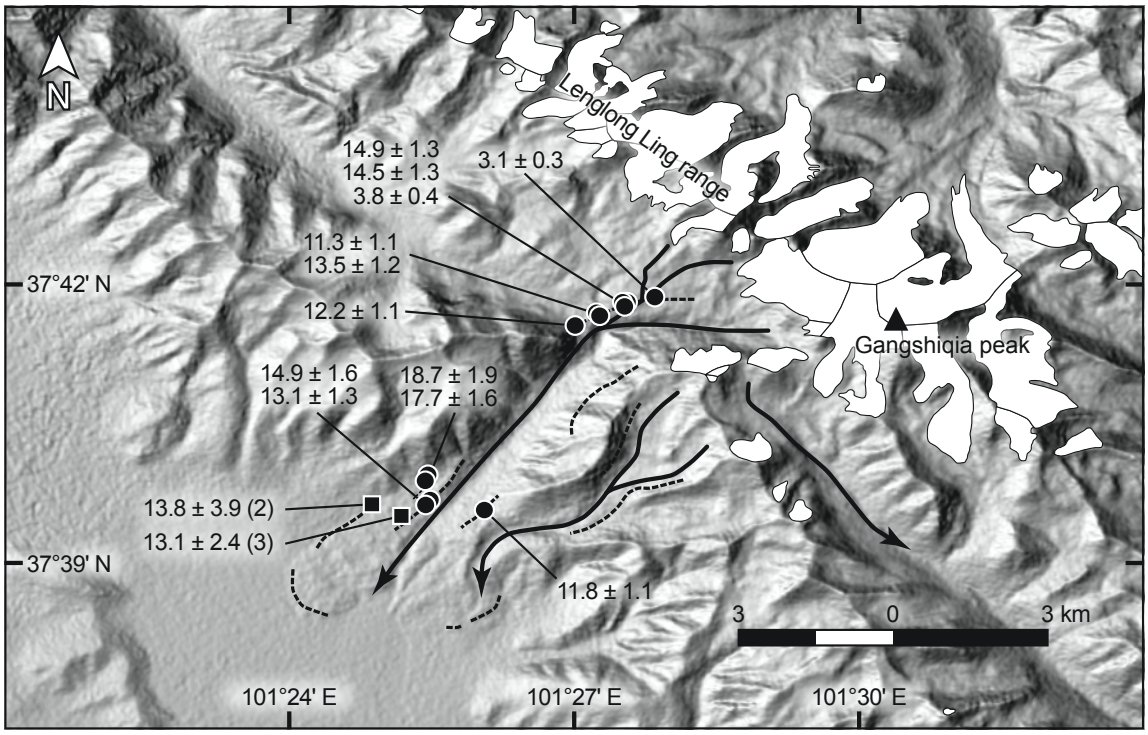

Figure 11. The Gangshiqia study site in the Qilian Shan. The dashed lines indicate moraine crests. The black arrows indicate the flow direction of the paleoglaciers. The circles indicate individual ^{10}Be ages, ka ± 1σ external uncertainty, reported in this study. The squares indicate mean ^{10}Be ages, ka ± 1σ total uncertainty (number of samples in the mean), calculated using data from Owen et al. (2003). The extent of modern glaciers (white polygons) is from RGI 6.0 (RGI Consortium, 2017). The background shaded relief image was constructed using Shuttle Radar Topography Mission (SRTM) 30-m-resolution digital elevation model data (1 arc-second global data; U.S. Geological Survey, 2018b).

and hosts large ice fields and their outlet glaciers today (Fig. 12). According to J. Heyman's compilation of exposure ages in the literature (http://expage.github.io), none of the moraines in the West Kunlun has been dated. The Aksaiqin site was located at the piedmont of Quanshui glacier (35.457°N, 80.389°E), an outlet glacier cresting at ~6350 m asl. Yasuda (2015) examined the terminus of the outlet glaciers around the study site using a series of Landsat satellite images to show that Quanshui glacier did not advance or retreat during 1972–2013, from which he classified the glacier as a nonsurging, climatically controlled "normal" glacier.

The subdued half-circular ridge ~6 km SW from the modern glacier tongue (Fig. 12B) may mark the local LGM extent of Quanshui glacier (*THAR* ELA ~5900 m asl). Two boulders from a distinct end moraine located ~3 km up valley from the lowest moraine (?) gave a mean ^{10}Be age of 31.1 ± 13.0 ka. The lowest moraine would correspond to a *THAR* ELA of 5966 m asl. The glacial lake below the glacier terminus is impounded behind an end moraine. A single boulder from the lower part of the end moraine was ^{10}Be-dated to 184.5 ± 17.5 ka. Two boulders collected from the upper part of the end moraine gave ^{10}Be ages of 15.5 ± 1.4 ka and 42.8 ± 3.8 ka. The large discrepancy between these ages does not permit us to confidently constrain the age of the moraine, but the ^{10}Be ages suggest that this moraine was formed before the Holocene. The *THAR* ELA was estimated to be 5974 m asl for this end moraine, which is an indistinguishable value from the ELA for the late Pleistocene moraine. The *THAR* ELA for the modern glacier was estimated as ~6000 m asl (summer T_{air} = –0.5 ± 1.1 °C; annual *ppt* ~120 mm), representing ~80% ΔELA_{norm}.

West Kunlun, Aksaiqin Lake

Meltwater from the glaciers identified as RGI60-13.53621 and RGI60-13.38107 in the RGI 6.0 drains to Aksaiqin lake. The lake surface currently stands at 4850 m asl. We collected three boulders from the paleoshorelines at 9, 13, and 25 m above the current lake level and ^{10}Be-dated them to 28.0 ± 2.6 ka, 13.5 ± 1.5 ka, and 32.7 ± 3.0 ka, respectively. The ^{10}Be ages suggest that the lake level has been relatively constant since the global LGM and therefore that the supply of meltwater from the glaciers may not have changed significantly as well. However, the large discrepancy among the ^{10}Be ages shows that more dating will be required to define a shoreline chronology. The sample of pebbles from the shoreline of Aksaiqin lake (LAS-1; Table 2) and four splits yielded ^{10}Be ages ranging from ca. 270 to ca. 9 ka (Fig.

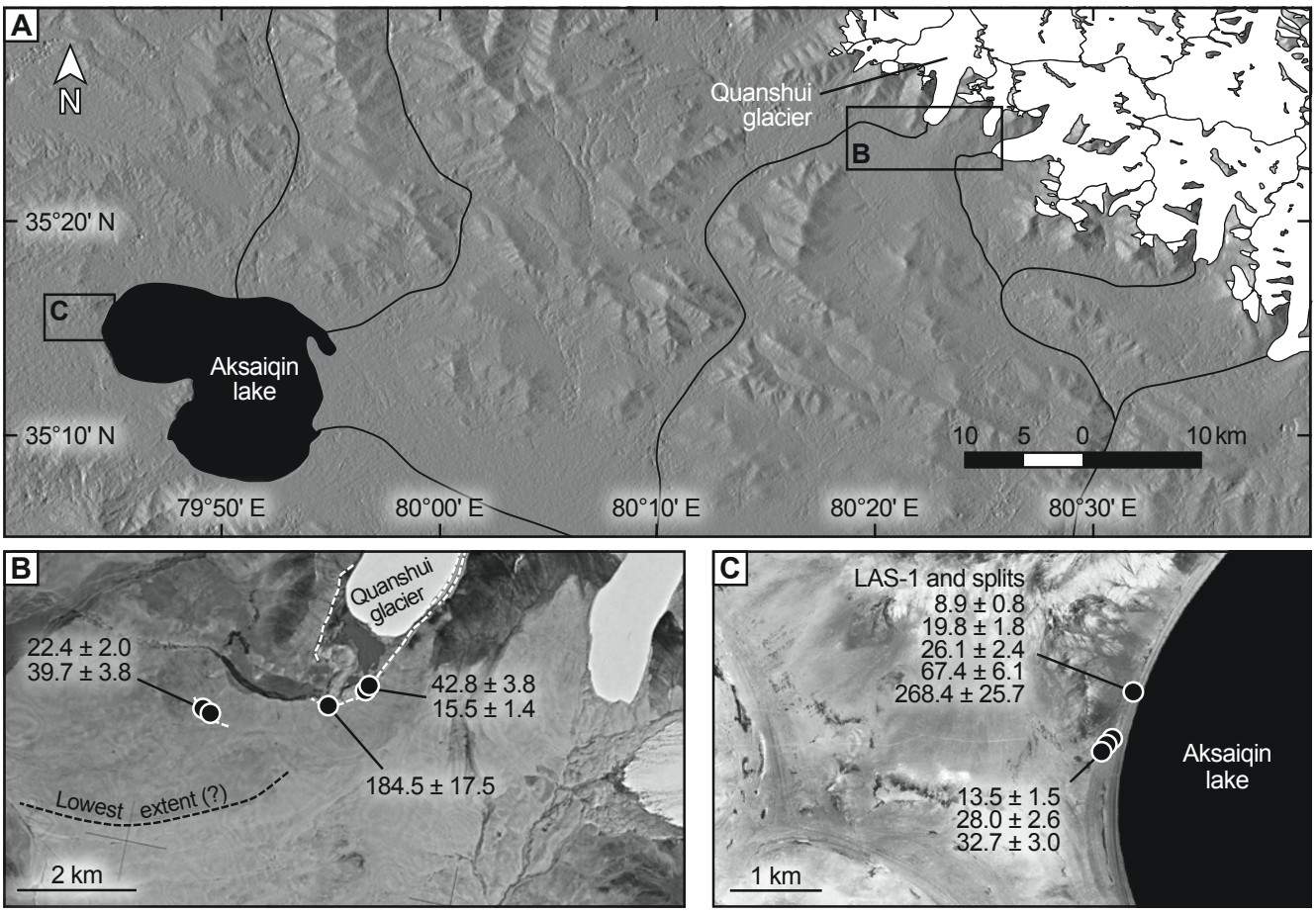

Figure 12. The study sites near Aksaiqin lake and Quanshui glacier in the West Kunlun, showing (A) extent of modern glaciers (white polygons; RGI 6.0; RGI Consortium, 2017), and rivers (black lines); (B) the moraine crests (dashed lines) and the ^{10}Be ages (circles), ka ± 1σ external uncertainty, reported in this study; and (C) western end of the Aksaiqin lake and the ^{10}Be ages (circles), ka ± 1σ external uncertainty, reported in this study. The background shaded relief image in A was constructed using Advanced Spaceborne Thermal Emission and Reflection Radiometer (ASTER) Global Digital Elevation Model (GDEM) V2 (NASA and METI, 2017). The background image in B is DISP/KH-9 photo acquired in 1980 (U.S. Geological Survey, 2018a), and background image in C is Google Earth, DigitalGlobe, image.

12C). The comparison of these ages suggests that pebble-to-pebble age differences are as great as the age differences among the amalgamated pebble samples from the adjacent shorelines. The low ^{26}Al/^{10}Be concentration ratios in the pebble samples, ranging from 5.82 to 4.34, except in sample LAS-3 (^{26}Al/^{10}Be = 7.03), suggest that the pebble samples may have been buried and re-exposed since their deposition.

West Kunlun, Karakax

At the end of the NW end of the West Kunlun, an ~60-km-long range stretches in an approximately W-E direction. It is heavily glaciated today. The Karakax study site was chosen at the mouths of two glaciated tributary valleys carved by two south-flowing large outlet glaciers emanating from a large ice field (Fig. 13). The paleoglacier in the eastern valley, termed Karakax-A (Fig. 13A), is sourced from at least seven cirque areas, and the paleoglacier in the western valley, termed Karakax-B, is sourced from at least four large cirque areas. The sediment-filled floor of Karakax-A (Figs. 13A and 13B) was ~350 m below the trimlines, which indicates the minimum thickness of the largest paleoglacier in the valley. The modern glacier in Karakax-B terminates at ~5180 m asl, ~80 m lower than the terminus of the glacier in Karakax-A. The fans in the valley, fed by outwash from the glaciers, extend ~6 km from the glacier termini. The fan was offset along the left-lateral strike-slip Altyn Tagh fault (Fig. S30 [see footnote 1]).

We sampled three boulders from the surface of the eastern margin of the fan and ^{10}Be-dated them to 90.2 ± 12.0 ka (mean after removing one outlier). The moraine crests deposited by the Karakax-B paleoglacier on the fans are preserved better above the Altyn Tagh fault than close to the valley floor. Two boulders from the right-lateral moraine gave a mean ^{10}Be age of 80.7 ± 13.3 ka; two boulders from the left-lateral moraine gave a similar

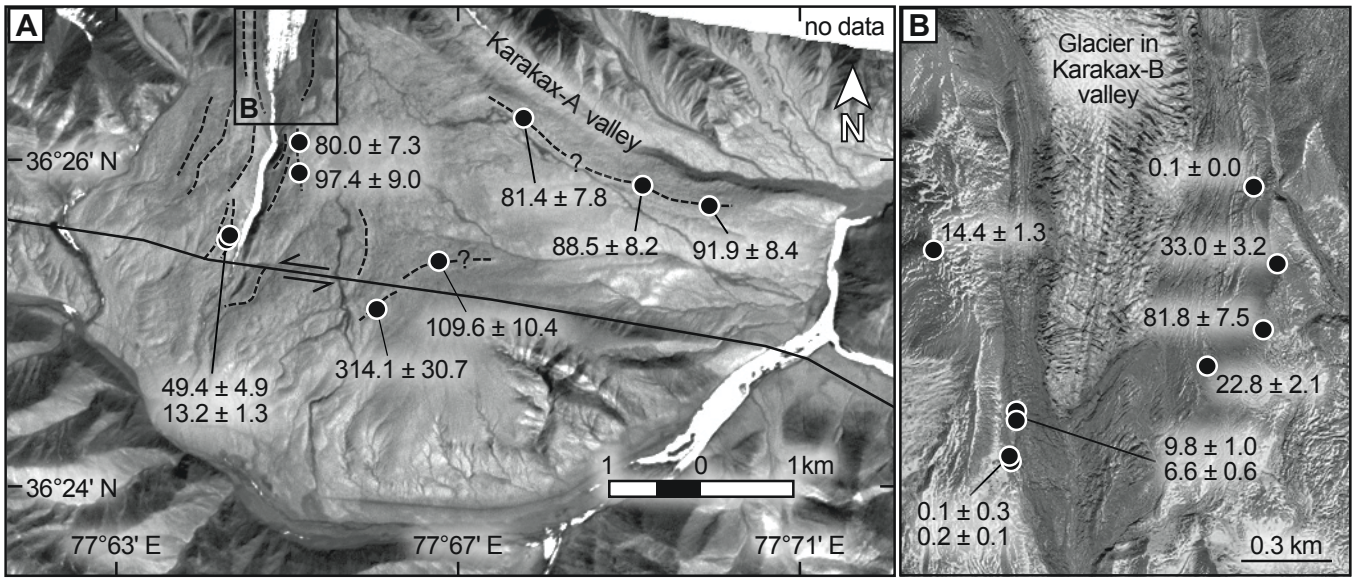

Figure 13. The Karakax study site in the West Kunlun showing (A) the modern glacier tongue, the moraine crests (dashed lines), the ^{10}Be ages (circles), ka ± 1σ external uncertainty, reported in this study, and the Altyn Tagh fault (white line with arrows indicating the slip), and (B) the ^{10}Be ages (circles), ka ± 1σ external uncertainty, reported in this study. The background images are Advanced Spaceborne Thermal Emission and Reflection Radiometer (ASTER) image (NASA and METI, 2001) in A and Google Earth, DigitalGlobe, image in B.

mean ^{10}Be age of 88.7 ± 16.9 ka. These near-maximum standstills of late MIS 5 are temporally asynchronous with the MIS 3 local LGM standstills of Aksaiqin paleoglaciers. However, a large erratic heavily eroded to a mushroom shape by wind (Figs. S28 and S29 [see footnote 1]) suggests that the ^{10}Be ages from Karakax should be considered as minimum ages unless corrected for boulder erosion. The modern glacier in Karakax-B valley, identified as RGI60–13.40092 in the RGI 6.0, has a *THAR* ELA of ~5720 m asl (summer T_{air} = 0.4 ± 1.0 °C; annual *ppt* ~170 mm). The lack of cobbles and boulders on the surfaces of other nearby fans along the Altyn Tagh fault was attributed to salt weathering in the upper 30 cm of the soil horizon (Farr and Chadwick, 1996). In addition, the existence of large gypsum and other soluble salt crystals and the lack of $CaCO_3$ in the soils away from riparian areas (Figs. S28 and S29 [see footnote 1]) provide evidence for hyperaridity in the region extending back for tens of thousands of years, suggesting that the glaciers there operated under low precipitation.

DISCUSSION

Modern and Paleo-ELA Gradients in Central Asia

The modern ELA and paleo-ELAs, ΔELA, and ΔELA_{norm} for MIS 2 glaciers in central Asia are plotted against latitude in Figure 14. The modern ELAs are mapped on a regional scale in Figure 15. A map of ΔELAs during MIS 2 is shown in Figure 16. The results of the ELA analysis and our interpretation for the timing of the local LGM glaciers are summarized in Figure 17.

Perhaps the most global factor driving the variations in climate is solar insolation and its variation across the latitudinal transect. The latitudinal gradients of modern and MIS 2 paleo-ELAs (Fig. 14) show strong correlations for both the modern ELAs (R^2 = 0.68) and for MIS 2 paleo-ELAs (R^2 = 0.91). The modern ELAs in central Asia decrease by ~120 m per 1° increase in latitude (Fig. 14A). During MIS 2, the latitudinal gradient of the paleo-ELAs was slightly steeper at ~160 m ELA decrease per 1° increase in latitude (Fig. 14A). This shift in the latitudinal gradient of paleo-ELAs during MIS 2, however, was largely derived from large ΔELAs for high latitude (50°N–45°N) glaciers and relatively smaller ΔELAs observed in midlatitudes, 45°N–35°N (Fig. 14B), highlighting the strong sensitivity of central Asian glaciers to local conditions.

The coldest peak of the global LGM, defined at ca. 21 ka by the modeling community (e.g., Braconnot et al., 2007) based on the marine oxygen-isotope records, is one of the best-studied periods of the last glacial cycle. Twelve general circulation models (GCMs) with various boundary conditions for global LGM showed a decrease in T_{air} everywhere in central Asia, with higher magnitudes of depression in high latitudes (Rupper and Koppes, 2010). It is consistent with the latitudinal gradient of the paleo-ELAs (Fig. 14A) for melt-dominated glaciers, indicating that T_{air} was indeed the controlling factor in their growth. However, many glaciers in the interior of central Asia exhibited smaller ΔELAs during MIS 2 (Figs. 14B–14C).

Annan and Hargreaves (2013) used GCMs to show that the T_{air} over all of central Asia was uniformly depressed by 8–4 °C, with an uncertainty of 4–2 °C, during the global LGM. The

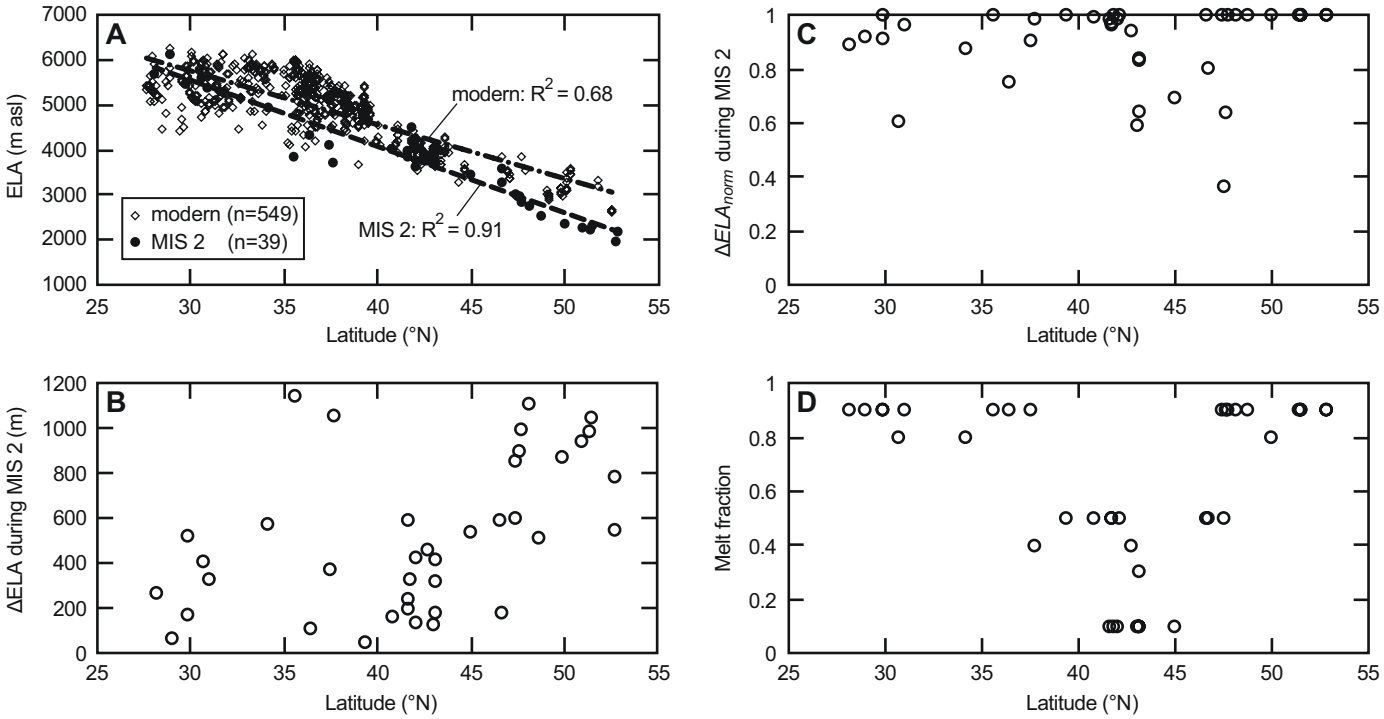

Figure 14. Latitudinal gradients of modern and marine oxygen-isotope stage (MIS) 2 equilibrium-line altitudes (ELAs): (A) modern ELAs (diamonds) and the paleo-ELAs for the dated MIS 2 standstills (closed circles); (B) ΔELA values for the dated MIS 2 standstills; (C) ΔELA_{norm} values for the dated MIS 2 standstills; and (D) melt fraction for the regions with the dated MIS 2 standstills (from Rupper and Roe, 2008). Modern and paleo-ELAs both show latitudinal gradients, implying that summer air temperature (T_{air}) and insolation are strong controls on glacier advances. However, ΔELA values do not exhibit a latitudinal gradient, suggesting that variable annual precipitation (*ppt*) affects the magnitudes of the glacier advances. For example, many sublimation-dominated glaciers in the interior of central Asia (45°N–40°N) did not advance to their local maximum despite the minimum in T_{air} and insolation during MIS 2. In general, plotting the data points onto a single line of latitude obscures the variability in *ppt* in the longitudinal direction, and a single N-S transect does not capture the details of the various conditions affecting the glacier mass balance.

multiproxy compilation by Yan et al. (2018) also suggested a T_{air} depression of 9–2 °C and a reduction of *ppt* compared to modern values by ~68%–33% during the global LGM. If we were to assume an unlikely condition that there was no change in *ppt* during MIS 2 from modern values, the observed ΔELAs for all MIS 2 glaciers considered in this study (mean 430 ± 320 m, 1σ) would indicate a mean T_{air} depressions of ~2.9 ± 1.9 °C (1σ), after using the regional atmospheric lapse rates of ~6.5 °C km^{-1} to correct for altitude. However, the map of ΔELAs during MIS 2 (Fig. 16) reveals a detailed pattern in the response of glaciers to the climate changes of MIS 2. The small ΔELAs observed in the interior of the continent are for sublimation-dominated glaciers (e.g., Fig. 14D). If the uniform T_{air} depression of 8–4 °C were true, the small ΔELAs would indicate that the sublimation-dominated glaciers were not sensitive to changes in T_{air}. In other words, the T_{air} depression of 8–4 °C during the global LGM would have resulted in ~1230–620 m ΔELAs, and the T_{air} alone cannot explain the small values of observed ΔELAs.

It is difficult to reliably model changes in *ppt* using GCMs, largely due to a variety of potential configurations that can be used to simulate the changes in the westerly storm tracks and South Asian monsoon (Rupper and Koppes, 2010). In the melt-dominated regions of central Asia, the ΔELAs were large (Fig. 16), ranging from ~500 m in the interior up to ~1100 m in the northern regions. The modeled T_{air} depressions would be expected to drive these large ΔELAs during MIS 2, even accounting for decrease in *ppt*, indicating that the glaciers are indeed good proxies for reconstructing T_{air} in melt-dominated regions. However, in the interior of central Asia, the modern glaciers are located at cold, high altitudes (Fig. 15), and many of them were limited to their cirques during MIS 2, showing small ΔELA_{norm} (Fig. 14C) and small ΔELAs (Fig. 16). In these cold, arid regions, a significant portion of the ablation is regulated by sublimation (Fig. 14D). In other words, sublimation could have ablated most of the additional accumulation in the prolonged cold seasons of MIS 2, and the glaciers would not have grown, even under large depressions of T_{air}. These sublimation-dominated glaciers can be useful to reconstruct paleo-*ppt* if the T_{air} is constrained from an independent proxy.

The timing of local LGM extents (ΔELA_{norm} ≥90%; Fig. 17) constructed from cosmic-ray exposure dating combined with mapping in the field and from satellite images reveals

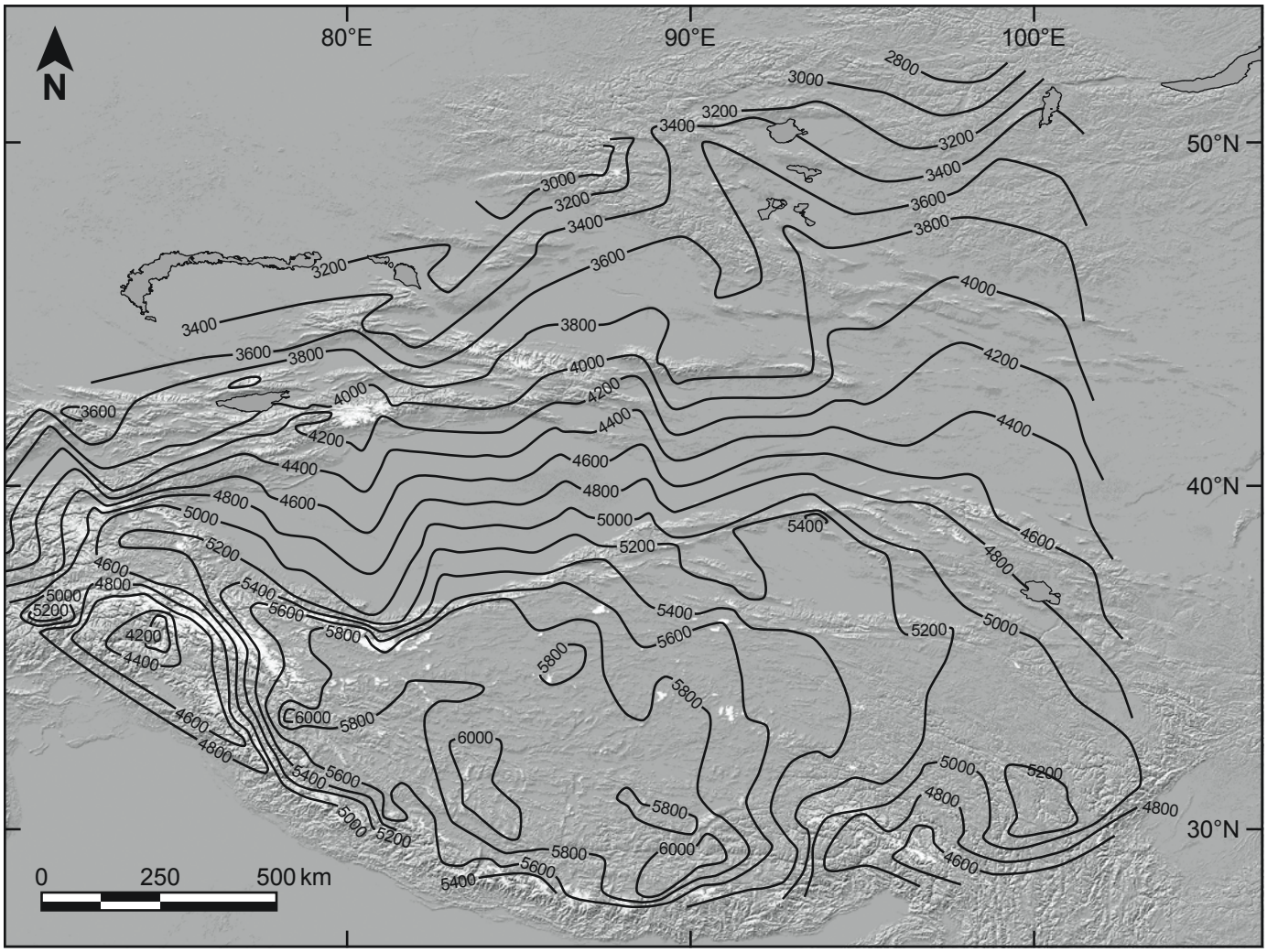

Figure 15. Map of modern equilibrium-line altitude (ELA in m asl) in central Asia. The extents of modern glaciers (white polygons) and their toe altitudes are from RGI 6.0 (RGI Consortium, 2017), and the toe-headwall altitude ratio (*THAR*) ELAs were estimated by using the headwall altitudes we measured in Google Earth. The contour lines were constructed with bilinear interpolation in QGIS. The glaciers in more humid regions along the margins of the continent are located at much lower altitudes compared to the glaciers in the interior, where arid climate limits the glaciers to the subfreezing temperatures of high altitudes. The shaded relief image in the background was constructed from Shuttle Radar Topography Mission (SRTM) digital elevation model data (GTOPO030; U.S. Geological Survey, 2017).

asynchronous temporal and spatial patterns of glaciations in central Asia. Approximately 20% of the 23 paleoglaciers with dated MIS 2 (29–14 ka) moraines did not extend to their local maxima, suggesting that they did not respond sensitively to the low insolation and low T_{air} of the global LGM. The remaining 23 paleoglaciers reached their local maxima ($\Delta ELA_{norm} \geq 90\%$) during MIS 5–3, despite the higher T_{air} during MIS 5–3 than during MIS 2. However, we note that these include the sites where the age uncertainty is larger than for MIS 2 (Table S10 [see footnote 1]). Relatively low values of melt fractions predicted in the regions where these MIS 5–3 glaciers were located and their subsequent smaller advances during MIS 2 indicate that the glaciers may have been precipitation-controlled features. In other words, increased *ppt* during MIS 3 may have provided additional accumulation and driven the glaciers to their local LGM extent, and later during MIS 2, a drier climate limited the accumulation despite the decreased T_{air}. These older glacial maxima were observed in regions with annual *ppt* ranging from ~310 to 110 mm.

Assumptions in the Use of ELA for Paleoclimate Reconstructions

An accurate reconstruction of T_{air} and *ppt* values from paleo-ELAs estimated from moraine locations depends on three fundamental assumptions: (1) The modern ELA, measured or estimated, is in equilibrium with the forcing climate factors. (2) The local modern lapse rate was similar in the past. (3) The sensitivity of a glacier to forcing climate factors was similar in the past.

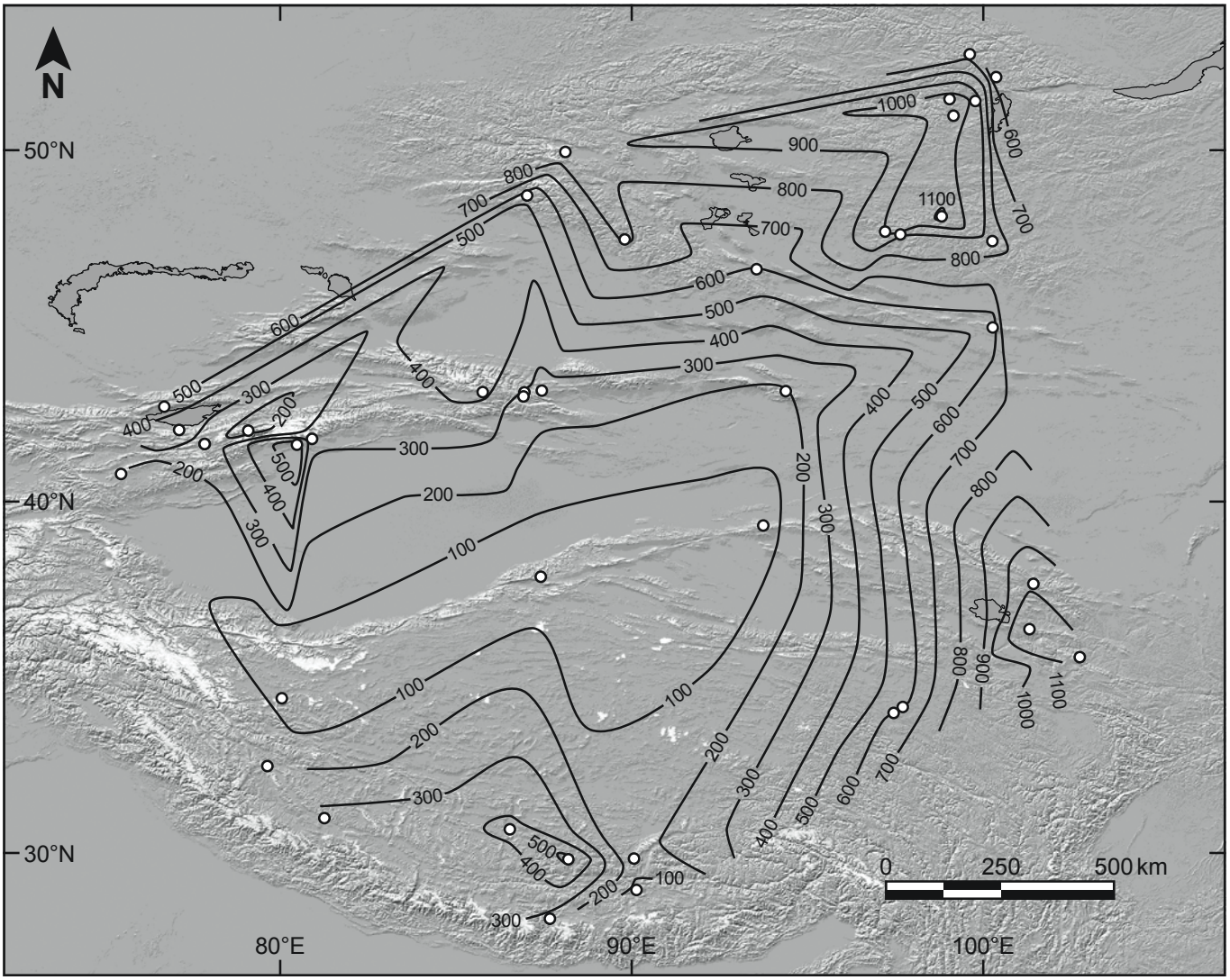

Figure 16. Map of marine oxygen-isotope stage (MIS) 2 maximum equilibrium-line altitude depressions (ΔELAs in m) in central Asia, based on the new ^{10}Be ages reported in this study and those from the literature. We estimated the paleo–toe-headwall altitude ratio (*THAR*) ELAs using the altitudes of the dated moraines, and we measured the headwall altitudes in Google Earth. The ΔELAs were then derived using the modern ELA data shown in Figure 14. The contour lines were constructed with bilinear interpolation in QGIS using the ΔELA data points (white dots). The extents of modern glaciers (white polygons) are from RGI 6.0 (RGI Consortium, 2017). The glaciers in the hyperarid interior of the continent exhibited the smallest ΔELAs. These sublimation-dominated glaciers are already located in high altitudes with much colder climates than those in more humid regions, and the large depression of summer air temperature (T_{air}) during MIS 2 was ineffective in driving the growth of these glaciers. The shaded relief image in the background was constructed from Shuttle Radar Topography Mission (SRTM) digital elevation model data (GTOPO30; U.S. Geological Survey, 2017).

Below, we will discuss the implications of these assumptions for reconstructing paleoclimate from paleo-ELA estimations.

Modern glaciers in central Asia are losing mass, as evident from direct measurements (summarized by Medvedeff and Roe, 2017) and from satellite measurements (summarized by Gardner et al., 2013). Aggregated data of glacier length measurements show that the observed glacier recessions for the past 30 yr were more than their natural variability, an indication that changes in climate have been driving the retreats (Roe et al., 2017). Numerical modeling of changes in glacier area suggests that ~25% of the recent shrinkage of glacier area has been due to anthropogenic climate warming (Marzeion et al., 2014). Comparison of the natural response time of glacier length change to climate variability has shown that the modern glaciers are in "disequilibrium" with the current climate, and further glacier retreats are inevitable, even if the climate stopped warming today (Christian et al., 2018). These evaluations strongly imply that the estimated modern ELAs are not steady-state ELAs, and therefore that

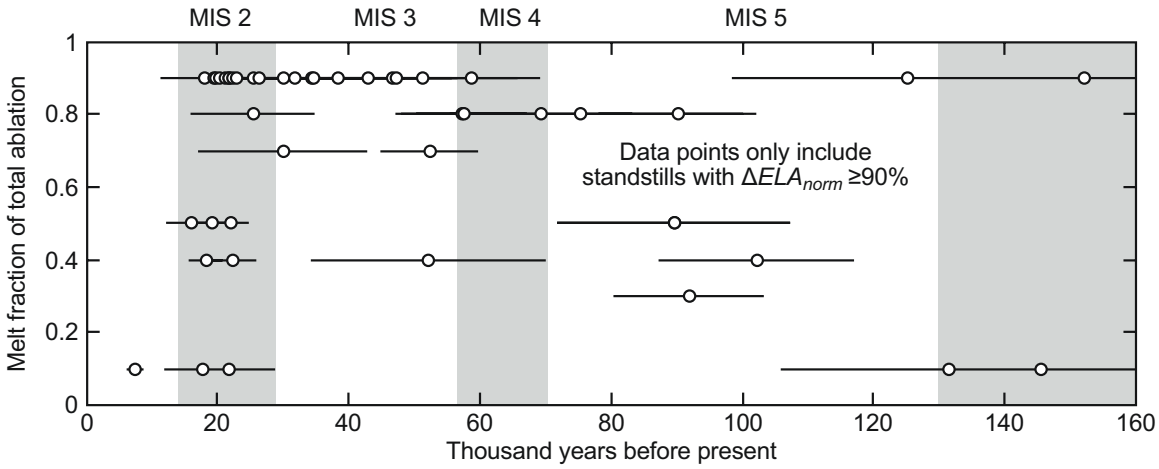

Figure 17. The predicted melt fraction for modern glaciers and the timing of the local last glacial maximum (LGM) standstills. A subset of 46 data points with normalized ELA depression (ΔELA_{norm}) ≥90% was extracted from Table S10 (see Supplemental Material [text footnote 1]). Half of these glaciers reached their local maxima during marine oxygen-isotope stage (MIS) 2, ~80% of which were predicted to have a melt fraction ≥0.5 (i.e., temperature-controlled features). The remaining half of the glaciers reached their local LGM standstills during MIS 5–3, much earlier than MIS 2, ~25% of which were predicted to have a melt fraction <0.5 (i.e., precipitation-controlled features).

climate variables estimated at the modern ELA may not be accurate for paleoclimate reconstructions. However, the ELA changes over the past 30 yr are on the order of tens of meters, and the estimated ΔELAs for MIS 5–2 glaciers are measured in hundreds of meters. We agree with Christian et al. (2018) that the paleoclimate inferences from Holocene glaciers require calibration of the estimated ΔELAs, but the large spatial and temporal changes in ELAs for MIS 5–2 glaciers represent large enough signals that their ΔELAs may be good proxies for reconstructing paleo-T_{air}. On the other hand, since the low ΔELAs for MIS 5–2 glaciers were mainly for precipitation-controlled glaciers, they may provide a new opportunity to reconstruct paleo-*ppt*, if the regional T_{air} depression can be determined from other independent proxies. In any case, the ΔELAs for MIS 5–2 glaciers are the observed responses to major changes in climate parameters, and the variety of ΔELAs observed in central Asia highlights the need to quantify the sensitivity of glaciers to climate parameters.

Temperature records at high altitudes and latitudes are sparse, and gridded reanalysis climate data sets tend to show bias toward lower altitudes. In turn, numerical modeling studies of glaciers using these T_{air} rely on atmospheric lapse rates of free air (usually 7–6 °C km^{-1}) to scale T_{air} to approximate the climate conditions at high altitudes. The T_{air} lapse rate used in the paleoclimate reconstruction from glaciers, however, can be a source of major uncertainty. For example, the lapse rate of summer T_{air} measured over maritime Canadian Arctic glaciers (~5 °C km^{-1}) was consistently lower than in free air (Gardner et al., 2009). Batbaatar et al. (2018) measured T_{air} ~2 m above a glacier surface in the Gobi-Altai to determine that the lapse rate there was ~8 °C km^{-1}, higher than a lapse rate of ~6.5 °C km^{-1} calculated from NCEP/NCAR reanalysis data (Kalnay et al., 1996), which we used in this study also. A combination of weather station data at low and high altitudes and numerical modeling showed that the windward side of the Cascade Range in Washington State exhibited much lower lapse rates of 5.2–3.9 °C km^{-1} (Minder et al., 2010). Gardner and Sharp (2009) recommended using different lapse rates for glacier mass-balance calculations depending on the region. In addition to the different modern values, the lapse rates also varied in the past, and there is no easy way to recover that information. One way to address this problem would be account for various lapse rates and compound the results with the uncertainties of the ΔELA values and the T_{air} values used for modern climate. For example, the JJA lapse rates estimated from the modern T_{air} (NCEP/NCAR; Kalnay et al., 1996) were uniform across central Asia with very little variation, at 6.5 ± 0.2 °C km^{-1}, and the range of ΔELAs for the glaciers surveyed in this study (430 ± 320 m) would indicate a T_{air}-depression range of 2.8 ± 2.0 °C (1σ). However, accounting for a lapse rate ranging from 7.5 to 5.5 °C km^{-1} would indicate a much wider range of T_{air} depressions (2.9 °C ± 6.4 °C), highlighting the large uncertainty in T_{air} reconstructions from glaciers and the stark differences in climates of central Asia.

The empirical curve between summer T_{air} and annual *ppt* at the modern ELA for the glaciers in central Asia (Fig. 2A; Sakai et al., 2015) was derived from glaciers with various local conditions, such as cirque orientation, slope, or rock type of the bed, all of which may exert a degree of control over glacier dynamics. The numerical sensitivity model of Rupper and Roe (2008) (see also Fig. 2B) also considered glaciers with various local conditions for calculations of melt fractions. These two diagrams demonstrate that the relationship between T_{air} and *ppt* at the ELA, regardless of the glaciers' geometric settings, is approximately linear in regions with >500 mm yr^{-1} *ppt*, suggesting that in the humid regions, the ELA sensitivities to T_{air} (∂ELA/∂T_{air}) and to

ppt (∂ELA/∂*ppt*) do not change when climate changes. In other words, glaciers will eventually equilibrate with a new climate, but the value of melt fraction on the curve of Rupper and Roe (2008) will remain >0.8, and the glacier under the new climate may acquire a new set of T_{air} and *ppt* values on the empirical curve of Sakai et al. (2015). However, in arid regions with <500 mm yr^{-1} *ppt*, the rate of change in T_{air} and *ppt* at the ELA ($\partial T_{air}/\partial ppt$) increases significantly (Fig. 2A), and a glacier may become more precipitation-controlled due to the larger proportion of sublimation in ablation (Fig. 2B). For example, the sensitivity analysis of glaciers in the Andes (Vargo et al., 2018) showed that ELA sensitivity of ~30 m per 1% increase in *ppt* for hyperarid regions approaches ~10 m per 1% increase in *ppt* when the annual *ppt* becomes >500 mm yr^{-1}. In their analysis, $\partial ELA/\partial T_{air}$ was similar, ~180 m $°C^{-1}$. In this case, T_{air} depression of 4 °C and no change in modern *ppt* would be enough to simulate the MIS 2 ΔELA of ~700 m observed in the humid regions of central Asia (Fig. 16). However, the MIS 2 ΔELA of <100 m observed in the interior regions of central Asia (Fig. 16) must be explained by an increase of annual *ppt* by ~30% of the modern value and/or much smaller ELA sensitivity to T_{air}. As sublimation becomes a more dominant process for ablation, ELA sensitivity to insolation becomes greater for glaciers in hyperarid regions than in the humid regions as well (Vargo et al., 2018), suggesting that the same amount of depression in insolation causes greater ΔELA for glaciers in the hyperarid regions than those in the humid regions. There are now large numbers of cosmic-ray exposure ages available for central Asian glaciers that developed under a variety of climate settings and their relative paleo-ELA values are useful to identify glaciers that are most sensitive to a climate variable of interest. Quantifying ELA sensitivities, however, remains the important issue for inferring paleoclimate from glacial evidence.

The heterogeneous patterns of glacier advances in central Asia have been noted before. Gillespie and Molnar (1995) emphasized the older and larger glacier advances than the global LGM advances and suggested that the increased precipitation and low temperatures were probably responsible for asynchronous glaciations in different regions. Rupper and Roe (2008) formulated a model to account for the role of sublimation in the ablation of glaciers and highlighted the regions where glaciers may be more sensitive to changes in *ppt* than to T_{air}. Hughes et al. (2013) surveyed local LGM advances throughout the world to show that the glacial maxima in central Asia occurred well before MIS 2, bringing the terminology of "Last Glacial Maximum" into question: Simply put, the maximum advances of glaciers in different regions or ranges did not occur at the same time, during the global LGM, or even during the same MIS. The timing of local LGM advances in central Asia and their corresponding melt fractions plotted in Figure 17 highlight that (1) most of the temperature-sensitive glaciers (high melt fraction) advanced to their maxima during MIS 3–2; (2) some precipitation-sensitive (low melt fraction) glaciers advanced to their maxima during MIS 5–4, and the subsequent advances during MIS 2 did not reach the older moraines; and (3) there is a high variability of melt fractions among the glaciers that reached their maxima during MIS 2, suggesting that the *ppt* change in central Asia was highly heterogenous and/or the melt fractions were underestimated for some of the glaciers.

An accurate inference about paleoclimate from glacial evidence depends on the recognition that the two important climate parameters to glacier mass balance, T_{air} and *ppt*, can vary independently through time, and the sensitivity of glacier mass balance to changes in them can also change through time. For example, the corresponding changes in glacier size as schematically plotted on the *x* (T_{air}) and *y* (*ppt*) axes in Figure 18 illustrate that similar ΔELAs observed in different regions can be explained by different magnitudes of changes in T_{air} and *ppt*. Similar extents of MIS 3 and MIS 2 glaciers in the humid regions of central Asia may be explained by reduced *ppt* during the global LGM, even though the T_{air} then was also lowered (arrow 1 in Fig. 18): The lower *ppt* would raise the ELA, but that tendency is countered by the lower T_{air}, which would lower the ELA. In arid settings, however, the T_{air} may be low enough that significant melt cannot occur, and the glacier mass balance is then dominated by sublimation. The glacier may retreat dramatically due to additional reduction of *ppt* (arrow 2 in Fig. 18), leaving MIS 2 glaciers in their cirques. During the transition from MIS 2 to MIS 1, T_{air} and *ppt* both increased (e.g., Herzschuh, 2006). A sublimation-dominated glacier under a modest increase of T_{air} would still be highly sensitive to *ppt*, and the glacier may grow even under increasing T_{air} (arrow 3 in Fig. 18; Batbaatar et al., 2018), whereas if the glaciers were melt dominated, then their high sensitivity to T_{air} would force them to retreat

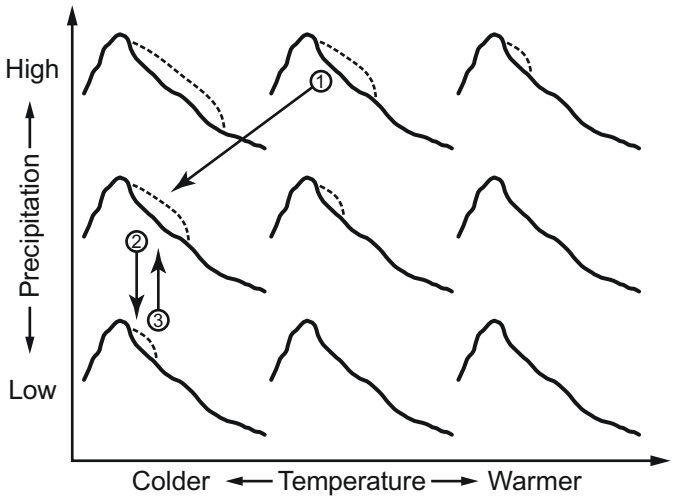

Figure 18. Schematic of glacier advance and retreat in response to changing climate. The two important climate variables for glacier mass balance, air temperature and precipitation, change in any direction in the schematic diagram. The equilibrium-line altitude depression (ΔELA) corresponding to changes in climate might differ depending on what direction the change is headed. For example, if the temperature gets colder in tandem with lowering precipitation (arrow 1), the corresponding ΔELA will be similar. The growth of glaciers with high sensitivity to precipitation, on the other hand, will be mostly dictated by changes in precipitation (arrows 2 and 3).

further. In the former case, the MIS 2 "global LGM" glacier may be no larger than the Holocene cirque glaciers. In this context, the observed heterogeneity in the pattern of glacier developments in central Asia provides an opportunity to evaluate paleoclimate reconstructions from independent proxies and/or validate numerical sensitivity analyses of glaciers in a continental setting.

CONCLUSIONS

We used cosmic-ray exposure dating to construct late Pleistocene and Holocene glacial chronologies and associated paleo-ELAs over a range of climatic conditions across central Asia. The regions considered in this study included the Altai, Tian Shan, Altyn Tagh, Qilian Shan, and Kunlun ranges, with large variability in summer temperatures, ranging from 7.6 °C to –2.2 °C, and annual precipitation ranging from 1020 to 65 mm. Regional-scale maps of both modern and paleo-ELAs show that the glaciers in central Asia exhibit highly heterogenous spatial and temporal patterns of glacier extents. Today, the ELAs range from ~6000 to ~3000 m asl in central Asia, with a consistent gradient across latitudes, indicating high sensitivity to air temperature. Indeed, most of the glaciers in central Asia are retreating due to the current regional warming trends, with the exception of the Kunlun region (Wang et al., 2018), where most of the annual precipitation falls in winter, and the snow accumulation there is less affected by warming (Kapnick et al., 2014). Of the 46 paleoglaciers that reached their all-time maxima (for the preserved record), half of them did so during MIS 2, suggesting that air temperature was a first-order factor controlling the glacier extents. However, the absolute values of ELA depression (ΔELA) of these paleoglaciers revealed a highly heterogeneous spatial pattern: Glaciers in the arid interior of central Asia exhibited ΔELAs of only 300–100 m, in contrast to glaciers in the humid regions of Altai and Qilian Shan, for example, which experienced ΔELAs of 1000–800 m. This is consistent with the numerical sensitivity analyses, which suggested that glaciers in arid regions are more sensitive to precipitation than those in humid regions. During MIS 5 and 3, periods with higher air temperature than during the global LGM, the paleoglaciers achieved their maximum extents, likely due to increased precipitation during these periods. The detailed mapping of observed spatial heterogeneity in glacial extents during MIS 2, and the temporal asynchrony of paleoglacier extents across central Asia highlight the complexities of inferring paleoclimate data from the glacial geomorphic record. An accurate reconstruction of paleoclimate parameters from former glacier extents, therefore, needs to be accompanied by numerical analysis of local glacier sensitivity to forcing climate parameters. The large scatter of cosmic-ray exposure ages from a single moraine and the resulting large total uncertainties (commonly 1σ ~30%–15%) of the age groups do not allow for a comparison of glacier activities within millennial time scales. Therefore, any direct connection between short climatic events, for example, the Little Ice Age or the Medieval Warm Period, and local glacier extents in central Asia must be established with caution.

ACKNOWLEDGMENTS

We are grateful to Dashnyam Sukhbaatar of "Damdin Da Foundation," Raymond Burke, Amgalan Bayasgalan, ZhongPing Lai, Shuji Wang, and Guijin Mu for logistical support and assistance in the field. We acknowledge John Stone, Paul Bierman, and Toshiyuki Fujioka for help in preparing and analyzing the samples, Anne B. Kahle for administrative support, Akiko Sakai for providing data from the Glacier Area Mapping for Discharge from the Asian Mountains (GAMDAM) inventory, and Yun Fan for providing elevation data for the Global Historical Climatology Network version 2 and Climate Anomaly Monitoring System (GHCN CAMS). Fieldwork and sample analysis were funded by the Quaternary Research Center, University of Washington, the Advanced Spaceborne Thermal Emission and Reflection Radiometer (ASTER) program of the National Aeronautics and Space Administration, and by a graduate research award to J. Batbaatar from the Department of Earth and Space Sciences, University of Washington. We thank B. Charlotte Schreiber and Taryn Black for careful reading of the early drafts. Careful and constructive reviews by two anonymous scholars and Glenn Thackray greatly improved our presentation.

REFERENCES CITED

Adler, R.F., Huffman, G.J., Chang, A., Ferraro, R., Xie, P., Janowiak, J., Rudolf, B., Schneider, U., Curtis, S., Bolvin, D., Gruber, A., Susskind, J., and Arkin, P., 2003, The Version 2 Global Precipitation Climatology Project (GPCP) Monthly Precipitation Analysis (1979–present): Journal of Hydrometeorology, v. 4, p. 1147–1167, https://doi.org/10.1175/1525-7541(2003)004<1147:TVGPCP>2.0.CO;2.

Anderson, L.S., Roe, G.H., and Anderson, R.S., 2014, The effects of interannual climate variability on the moraine record: Geology, v. 42, no. 1, p. 55–58, https://doi.org/10.1130/G34791.1.

Annan, J.D., and Hargreaves, J.C., 2013, A new global reconstruction of temperature changes at the Last Glacial Maximum: Climate of the Past, v. 9, p. 367–376, https://doi.org/10.5194/cp-9-367-2013.

Araguás-Araguás, L., Froehlich, K., and Rozanski, K., 1998, Stable isotope composition of precipitation over Southeast Asia: Journal of Geophysical Research, v. 103, p. 28,721–28,742, https://doi.org/10.1029/98JD02582.

Balco, G., 2016, Let a Hundred Flowers Bloom: The Bleeding Edge of Cosmogenic-Nuclide Geochemistry: https://cosmognosis.wordpress.com/2016/08/01/let-a-hundred-flowers-bloom/ (accessed March 2018).

Balco, G., Stone, J.O., Lifton, N.A., and Dunai, T.J., 2008, A complete and easily accessible means of calculating surface exposure ages or erosion rates from ^{10}Be and ^{26}Al measurements: Quaternary Geochronology, v. 3, p. 174–195, https://doi.org/10.1016/j.quageo.2007.12.001.

Batbaatar, J., and Gillespie, A., 2016, Outburst floods of the Maly Yenisei. Part II: New age constraints from Darhad basin: International Geology Review, v. 58, no. 14, p. 1753–1779, https://doi.org/10.1080/00206814.2016.1193452.

Batbaatar, J., Gillespie, A., Fink, D., Matmon, A., and Fujioka, T., 2018, Asynchronous glaciations in arid continental climate: Quaternary Science Reviews, v. 182, p. 1–19, https://doi.org/10.1016/j.quascirev.2017.12.001.

Benn, D.I., and Lehmkuhl, F., 2000, Mass balance and equilibrium-line altitudes of glaciers in high-mountain environments: Quaternary International, v. 65–66, p. 15–29, https://doi.org/10.1016/S1040-6182(99)00034-8.

Benn, D.I., and Owen, L.A., 1998, The role of the Indian summer monsoon and the mid-latitude westerlies in Himalayan glaciation: Review and speculative discussion: Journal of the Geological Society, v. 155, p. 353–363, https://doi.org/10.1144/gsjgs.155.2.0353.

Benn, D., Owen, L.A., Osmaston, H.A., Seltzer, G.O., Porter, S.C., and Mark, B., 2005, Reconstruction of equilibrium-line altitudes for tropical and sub-tropical glaciers: Quaternary International, v. 138–139, p. 8–21, https://doi.org/10.1016/j.quaint.2005.02.003.

Blomdin, R., Stroeven, A.P., Harbor, J.M., Lifton, N.A., Heyman, J., Gribenski, N., Petrakov, D.A., Caffee, M.W., Ivanov, M.N., Hättestrand, C., and Rogozhina, I., 2016, Evaluating the timing of former glacier expansions in the Tian Shan: A key step towards robust spatial correlations: Quaternary Science Reviews, v. 153, p. 78–96, https://doi.org/10.1016/j.quascirev.2016.07.029.

Borchers, B., Marrero, S., Balco, G., Caffee, M., Goehring, B., Lifton, N., Nishiizumi, K., Phillips, F., Schaefer, J., and Stone, J., 2016, Geological calibration of spallation production rates in the CRONUS-Earth project: Quaternary Geochronology, v. 31, p. 188–198, https://doi.org/10.1016/j.quageo.2015.01.009.

Braconnot, P., Otto-Bliesner, B., Harrison, S., Joussaume, S., Peterchmitt, J.-Y., Abe-Ouchi, A., Crucifix, M., Driesschaert, E., Fichefet, T., Hewitt, C.D., Kageyama, M., Kitoh, A., Laîné, A., Loutre, M.-F., Marti, O., Merkel, U., Ramstein, G., Valdes, P., Weber, S.L., Yu, Y., and Zhao, Y., 2007, Results of PMIP2 coupled simulations of the Mid-Holocene and Last Glacial Maximum—Part 1: experiments and large-scale features: Climate of the Past, v. 3, p. 261–277, https://doi.org/10.5194/cp-3-261-2007.

Chauvenet, W., 1891, Method of least squares, *in* Chauvenet, W., A Manual of Spherical and Practical Astronomy. Volume II: Theory and Use of Astronomical Instruments (5th ed., rev. and corr.): Philadelphia, J.B. Lippincott Co., p. 558–566.

Christian, J.E., Koutnik, M., and Roe, G., 2018, Committed retreat: Controls on glacier disequilibrium in a warming climate: Journal of Glaciology, v. 64, p. 675–688, https://doi.org/10.1017/jog.2018.57.

Clark, P.U., Dyke, A.S., Shakun, J.D., Carlson, A.E., Clark, J., Wohlfarth, B., Mitrovica, J.X., Hostetler, S.W., and McCabe, A.M., 2009, The Last Glacial Maximum: Science, v. 325, p. 710–714, https://doi.org/10.1126/science.1172873.

Fan, Y., and van den Dool, H., 2008, A global monthly land surface air temperature analysis for 1948–present: Journal of Geophysical Research, v. 113, D01103, https://doi.org/10.1029/2007JD008470.

Farr, T.G., and Chadwick, O.A., 1996, Geomorphic processes and remote sensing signatures of alluvial fans in the Kun Lun Mountains, China: Journal of Geophysical Research, v. 101, p. 23,091–23,100, https://doi.org/10.1029/96JE01603.

Fedotov, A.P., and 15 others, 2004, Changes in the volume and salinity of Lake Khubsugul (Mongolia) in response to global climate changes in the Upper Pleistocene and the Holocene: Palaeogeography, Palaeoclimatology, Palaeoecology, v. 209, p. 245–257, https://doi.org/10.1016/j.palaeo.2003.12.022.

Fink, D., and Smith, A., 2007, An inter-comparison of ^{10}Be and ^{26}Al AMS reference standards and the ^{10}Be half-life: Nuclear Instruments & Methods in Physics Research, Section B, Beam Interactions with Materials and Atoms, v. 259, p. 600–609, https://doi.org/10.1016/j.nimb.2007.01.299.

Gardner, A.S., and Sharp, M., 2009, Sensitivity of net mass-balance estimates to near-surface temperature lapse rates when employing the degree-day method to estimate glacier melt: Annals of Glaciology, v. 50, p. 80–86, https://doi.org/10.3189/172756409787769663.

Gardner, A.S., Sharp, M.J., Koerner, R.M., Labine, C., Boon, S., Marshall, S.J., Burgess, D.O., and Lewis, D., 2009, Near-surface temperature lapse rates over arctic glaciers and their implications for temperature downscaling: Journal of Climate, v. 22, no. 16, p. 4281–4298, https://doi.org/10.1175/2009JCLI2845.1.

Gardner, A.S., Moholdt, G., Cogley, J.G., Wouters, B., Arendt, A.A., Wahr, J., Berthier, E., Hock, R., Pfeffer, W.T., Kaser, G., Ligtenberg, S.R.M., Bolch, T., Sharp, M.J., Hagen, J.O., van den Broeke, M.R., and Paul, F., 2013, A reconciled estimate of glacier contributions to sea-level rise: 2003 to 2009: Science, v. 340, p. 852–857, https://doi.org/10.1126/science.1234532.

Gillespie, A.R., 1991, Testing a new climatic interpretation for the Tahoe glaciation, *in* Hall, C.A., Jr., Doyle-Jones, V., and Widawski, B., eds., Natural History of Eastern California and High-Altitude Research: Proceedings of the White Mountain Research Station Symposium 3: Bishop, California, White Mountain Research Station, p. 383–398.

Gillespie, A., and Molnar, P., 1995, Asynchronous maximum advances of mountain and continental glaciers: Reviews of Geophysics, v. 33, p. 311–364, https://doi.org/10.1029/95RG00995.

Global Terrestrial Network for Glaciers (GTN-G), 2017, GTN-G Glacier Regions: Global Terrestrial Network for Glaciers, https://doi.org/10.5904/gtng-glacreg-2017-07 (accessed March 2018).

Google Earth, 2017, DigitalGlobe, CNES/Airbus: Google Earth Pro v. 7.3.2.5491, https://earth.google.com (accessed in 2017).

Gribenski, N., Jansson, K.N., Lukas, S., Stroeven, A.P., Harbor, J.M., Blomdin, R., Ivanov, M.N., Heyman, J., Petrakov, D.A., Rudoy, R., Clifton, T., Lifton, N.A., and Caffee, M.W., 2016, Complex patterns of glacier advances during the late glacial in the Chagan Uzun Valley, Russian Altai: Quaternary Science Reviews, v. 149, p. 288–305, https://doi.org/10.1016/j.quascirev.2016.07.032.

Gribenski, N., Jansson, K.N., Preusser, F., Harbor, J.M., Stroeven, A.P., Trauerstein, M., Blomdin, R., Heyman, J., Caffee, M.W., Lifton, N.A., and Zhang, W., 2018, Re-evaluation of MIS 3 glaciation using cosmogenic radionuclide and single grain luminescence ages, Kanas Valley, Chinese Altai: Journal of Quaternary Science, v. 33, p. 55–67, https://doi.org/10.1002/jqs.2998.

Grunert, J., Lehmkuhl, F., and Walther, M., 2000, Paleoclimatic evolution of the Uvs Nuur basin and adjacent areas (western Mongolia): Quaternary International, v. 65–66, p. 171–192, https://doi.org/10.1016/S1040-6182(99)00043-9.

Herzschuh, U., 2006, Palaeo-moisture evolution in monsoonal Central Asia during the last 50,000 years: Quaternary Science Reviews, v. 25, p. 163–178, https://doi.org/10.1016/j.quascirev.2005.02.006.

Heyman, J., 2014, Paleoglaciation of the Tibetan Plateau and surrounding mountains based on exposure ages and ELA depression estimates: Quaternary Science Reviews, v. 91, p. 30–41, https://doi.org/10.1016/j.quascirev.2014.03.018.

Heyman, J., 2018, A Global Compilation of Glacial ^{10}Be and ^{26}Al Data: http://expage.github.io/data/expage/expage-201803.txt (accessed March 2018).

Hubert-Ferrari, A., Suppe, J., Van Der Woerd, J., Wang, X., and Lu, H., 2005, Irregular earthquake cycle along the southern Tianshan front, Aksu area, China: Journal of Geophysical Research–Solid Earth, v. 110, B06402, https://doi.org/10.1029/2003JB002603.

Hughes, P.D., Gibbard, P.L., and Ehlers, J., 2013, Timing of glaciation during the last glacial cycle: Evaluating the concept of a global 'Last Glacial Maximum' (LGM): Earth-Science Reviews, v. 125, p. 171–198, https://doi.org/10.1016/j.earscirev.2013.07.003.

Kalnay, E., Kanamitsu, M., Kistler, R., Collins, W., Deaven, D., Derber, J., Gandin, L., Saha, S., White, G., Woollen, J., Zhu, Y., Chelliah, M., Ebisuzaki, W., Higgins, W., Janowiak, J., Mo, K.C., Ropelewski, C., Wang, J., Leetma, A., Reynolds, R., and Jenne, R., 1996, The NCEP/NCAR 40-year re-analysis project: Bulletin of the American Meteorological Society, v. 77, p. 437–471, https://doi.org/10.1175/1520-0477(1996)077<0437:TNYRP>2.0.CO;2.

Kapnick, S.B., Delworth, T.L., Ashfaq, M., Malyshev, S., and Milly, P.C.D., 2014, Snowfall less sensitive to warming in Karakoram than in Himalayas due to a unique seasonal cycle: Nature Geoscience, v. 7, p. 834–840, https://doi.org/10.1038/ngeo2269.

Komatsu, G., Brantingham, P.J., Olsen, J.W., and Baker, V.R., 2001, Paleoshoreline geomorphology of Böön Tsagaan Nuur, Tsagaan Nuur and Orog Nuur: The Valley of Lakes, Mongolia: Geomorphology, v. 39, p. 83–98, https://doi.org/10.1016/S0169-555X(00)00095-7.

Kong, P., Fink, D., Na, C.G., and Huang, F.X., 2009, Late Quaternary glaciation of the Tianshan, Central Asia, using cosmogenic ^{10}Be surface exposure dating: Quaternary Research, v. 72, p. 229–233, https://doi.org/10.1016/j.yqres.2009.06.002.

Koppes, M., Gillespie, A.R., Burke, R.M., Thompson, S.C., and Stone, J., 2008, Late Quaternary glaciation in the Kyrgyz Tien Shan: Quaternary Science Reviews, v. 27, p. 846–866, https://doi.org/10.1016/j.quascirev.2008.01.009.

Kraaijenbrink, P.D.A., Bierkens, M.F.P., Lutz, A.F., and Immerzeel, W.W., 2017, Impact of a global temperature rise of 1.5 degrees Celsius on Asia's glaciers: Nature, v. 549, p. 257–260, https://doi.org/10.1038/nature23878.

Lal, D., 1991, Cosmic ray labeling of erosion surfaces: In situ nuclide production rates and erosion models: Earth and Planetary Science Letters, v. 104, p. 424–439, https://doi.org/10.1016/0012-821X(91)90220-C.

Li, Y.K., Liu, G.N., Kong, P., Harbor, J., Chen, Y.X., and Caffee, M., 2011, Cosmogenic nuclide constraints on glacial chronology in the source area of the Urumqi River, Tian Shan, China: Journal of Quaternary Science, v. 26, p. 297–304, https://doi.org/10.1002/jqs.1454.

Li, Y.K., Liu, G.N., Chen, Y.X., Li, Y.N., Harbor, J., Stroeven, A.P., Caffee, M., Zhang, M., Li, C.C., and Cui, Z.J., 2014, Timing and extent of Quaternary glaciations in the Tianger Range, eastern Tian Shan, China, investigated using ^{10}Be surface exposure dating: Quaternary Science Reviews, v. 98, p. 7–23, https://doi.org/10.1016/j.quascirev.2014.05.009.

Lifton, N., Beel, C., Hättestrand, C., Kassab, C., Rogozhina, I., Heermance, R., Oskin, M., Burbank, D., Blomdin, R., Gribenski, N., Caffee, M., Goehring, B.M., Heyman, J., Ivanov, M., Li, Y.N., Li, Y.K., Petrakov, D., Usubaliev, R., Codilean, A.T., Chen, Y.X., Harbor, J., and Stroeven, A.P.,

2014, Constraints on the late Quaternary glacial history of the Inylchek and Sary-Dzaz valleys from in situ cosmogenic ^{10}Be and ^{26}Al, eastern Kyrgyz Tian Shan: Quaternary Science Reviews, v. 101, p. 77–90, https://doi.org/10.1016/j.quascirev.2014.06.032.

Lisiecki, L.E., and Raymo, M.E., 2005, A Pliocene-Pleistocene stack of 57 globally distributed benthic δ^{18}O records: Paleoceanography, v. 20, PA1003, https://doi.org/10.1029/2004PA001071.

Marzeion, B., Cogley, J.G., Richter, K., and Parkes, D., 2014, Attribution of global glacier mass loss to anthropogenic and natural causes: Science, v. 345, p. 919–921 https://doi.org/10.1126/science.1254702.

Medwedeff, W.G., and Roe, G.H., 2017, Trends and variability in the global dataset of glacier mass balance: Climate Dynamics, v. 48, p. 3085, https://doi.org/10.1007/s00382-016-3253-x.

Meierding, T.C., 1982, Late Pleistocene glacial equilibrium-line altitudes in the Colorado Front Range: A comparison of methods: Quaternary Research, v. 18, p. 289–310, https://doi.org/10.1016/0033-5894(82)90076-X.

Minder, J.R., Mote, P.W., and Lundquist, J.D., 2010, Surface temperature lapse rates over complex terrain: Lessons from the Cascade Mountains: Journal of Geophysical Research, v. 115, D14122, https://doi.org/10.1029/2009JD013493.

Mölg, T., and Hardy, D.R., 2004, Ablation and associated energy balance of a horizontal glacier surface on Kilimanjaro: Journal of Geophysical Research, v. 109, D16104, https://doi.org/10.1029/2003JD004338.

National Aeronautics and Space Administration (NASA), and The Ministry of Economy, Trade, and Industry (METI) of Japan, 2001, Advanced Spaceborne Thermal Emission and Reflection Radiometer (ASTER) Level 1B Data Set Registered Radiance at the Sensor: https://earthdata.nasa.gov (accessed March 2017 from NASA EOSDIS Land Processes DAAC).

National Aeronautics and Space Administration (NASA), and The Ministry of Economy, Trade, and Industry (METI) of Japan, 2017, Advanced Spaceborne Thermal Emission and Reflection Radiometer (ASTER) Global Digital Elevation Model Version 2 (GDEM V2): https://earthdata.nasa.gov (accessed September 2017).

Nishiizumi, K., 2004, Preparation of ^{26}Al AMS standards: Nuclear Instruments & Methods in Physics Research, Section B, Beam Interactions with Materials and Atoms, v. 223–224, p. 388–392, https://doi.org/10.1016/j.nimb.2004.04.075.

Nishiizumi, K., Imamura, M., Caffee, M.W., Southon, J.R., Finkel, R.C., and McAninch, J., 2007, Absolute calibration of ^{10}Be AMS standards: Nuclear Instruments & Methods in Physics Research, Section B, Beam Interactions with Materials and Atoms, v. 258, p. 403–413, https://doi.org/10.1016/j.nimb.2007.01.297.

Ohmura, A., Kasser, P., and Funk, M., 1992, Climate at the equilibrium line of glaciers: Journal of Glaciology, v. 38, p. 397–411, https://doi.org/10.1017/S0022143000002276.

Owen, L.A., and Benn, D.I., 2005, Equilibrium-line altitudes of the Last Glacial Maximum for the Himalaya and Tibet: An assessment and evaluation of results: Quaternary International, v. 138–139, p. 55–78, https://doi.org/10.1016/j.quaint.2005.02.006.

Owen, L.A., Ma, H.Z., Derbyshire, E., Spencer, J.Q., Barnard, P.L., Nian, Z.Y., Finkel, R.C., and Caffee, M.W., 2003, The timing and style of late Quaternary glaciation in the La Ji Mountains, NE Tibet: Evidence for restricted glaciation during the latter part of the last glacial: Zeitschrift für Geomorphologie Supplementband, v. 130, p. 263–276.

Peel, M.C., McMahon, T.A., Finlayson, B.L., and Watson, F.G.R., 2001, Identification and explanation of continental differences in the variability of annual runoff: Journal of Hydrology (Amsterdam), v. 250, p. 224–240, https://doi.org/10.1016/S0022-1694(01)00438-3.

Porter, S.C., 1975, Equilibrium-line altitudes of late Quaternary glaciers in the Southern Alps, New Zealand: Quaternary Research, v. 5, p. 27–47, https://doi.org/10.1016/0033-5894(75)90047-2.

Porter, S.C., 2000, Snowline depression in the tropics during the last glaciation: Quaternary Science Reviews, v. 20, p. 1067–1091, https://doi.org/10.1016/S0277-3791(00)00178-5.

Randolph Glacier Inventory (RGI) Consortium, 2017, Randolph Glacier Inventory—A Dataset of Global Glacier Outlines: Version 6.0: Technical Report, Global Land Ice Measurements from Space, Colorado, USA: https://doi.org/10.7265/N5-RGI-60 (accessed March 2018).

Reuther, A.U., 2007, Surface exposure dating of glacial deposits from the last glacial cycle: Evidence from the eastern Alps, the Bavarian Forest, the southern Carpathians and the Altai Mountains: Relief Boden Paläoklima, v. 21, 213 p.

Reuther, A.U., Herget, J., Ivy-Ochs, S., Borodavko, P., Kubik, P.W., and Heine, K., 2006, Constraining the timing of the most recent cataclysmic flood event from ice-dammed lakes in the Russian Altai Mountains, Siberia, using cosmogenic in situ ^{10}Be: Geology, v. 34, p. 913–916, https://doi.org/10.1130/G22755A.1.

Roe, G.H., Baker, M.B., and Herla, F., 2017, Centennial glacier retreat as categorical evidence of regional climate change: Nature Geoscience, v. 10, p. 95–99, https://doi.org/10.1038/ngeo2863.

Ross, S.M., 2003, Peirce's criterion for the elimination of suspect experimental data: Journal of Engineering Technology, v. 20, p. 38–41, http://classes.engineering.wustl.edu/2009/fall/che473/handouts/OutlierRejection.pdf.

Rupper, S., 2007, Glacier Sensitivity and Regional Climate: Past and Present [Ph.D. diss.]: Seattle, Washington, University of Washington, 204 p.

Rupper, S., and Koppes, M., 2010, Spatial patterns in Central Asian climate and equilibrium line altitudes: IOP Earth and Environmental Sciences, v. 9, 012009, https://iopscience.iop.org/article/10.1088/1755-1315/9/1/012009.

Rupper, S., and Roe, G., 2008, Glacier changes and regional climate: A mass and energy balance approach: Journal of Climate, v. 21, p. 5384–5401, https://doi.org/10.1175/2008JCLI2219.1.

Sakai, A., Nuimura, T., Fujita, K., Takenaka, S., Nagai, H., and Lamsal, D., 2015, Climate regime of Asian glaciers revealed by GAMDAM glacier inventory: The Cryosphere, v. 9, p. 865–880, https://doi.org/10.5194/tc-9-865-2015.

Shea, J.M., and Immerzeel, W.W., 2016, An assessment of basin-scale glaciological and hydrological sensitivities in the Hindu Kush–Himalaya: Annals of Glaciology, v. 57, p. 308–318, https://doi.org/10.3189/2016AoG71A073.

Shean, D., 2017, High Mountain Asia 8-Meter DEMs Derived from Along-Track Optical Imagery, Version 1: Boulder, Colorado, NASA National Snow and Ice Data Center Distributed Active Archive Center, https://doi.org/10.5067/GSACB044M4PK (accessed January 2019).

Stone, J.O., 2000, Air pressure and cosmogenic isotope production: Journal of Geophysical Research–Solid Earth, v. 105, p. 23,753–23,759, https://doi.org/10.1029/2000JB900181.

Thompson, L.G., Mosley-Thompson, E., Davis, M.E., Bolzan, J.F., Dai, J., Yao, T., Gundestrup, N., Wu, X., Klein, L., and Xie, Z., 1989, Holocene–late Pleistocene climatic ice core records from Qinghai-Tibetan Plateau: Science, v. 246, p. 474–477, https://doi.org/10.1126/science.246.4929.474.

U.S. Geological Survey, 2017, Global 30 Arc-Second Elevation (GTOPO30): Sioux Falls, South Dakota, Land Processes Distributed Active Archive Center located at USGS/EROS, http://lpdaac.usgs.gov (accessed March 2018).

U.S. Geological Survey, 2018a, Declassified military intelligence photographs from the *Keyhole* (KH) satellite system KH-9 (Hexagon) in digital format: Image ID DZB1216–500329L001001, acquisition date September 8, 1980: https://earthexplorer.usgs.gov (accessed March 2018).

U.S. Geological Survey, 2018b, USGS EROS Archive—Digital Elevation Shuttle Radar Topography Mission (SRTM) 1 Arc-Second Global: https://earthexplorer.usgs.gov (accessed March 2018).

U.S. Geological Survey Geological Names Committee, 2010, Divisions of Geologic Time—Major Chronostratigraphic and Geochronologic Units: U.S. Geological Survey Fact Sheet 2010-3059, 2 p., https://pubs.usgs.gov/fs/2010/3059/.

Vargo, L.J., Galewsky, J., Rupper, S., and Ward, D.J., 2018, Sensitivity of glaciation in the arid subtropical Andes to changes in temperature, precipitation, and solar radiation: Global and Planetary Change, v. 163, p. 86–96, https://doi.org/10.1016/j.gloplacha.2018.02.006.

Wang, Y., Hou, Sh., Huai, B., An, W., Pang, H., and Liu, Y., 2018, Glacier anomaly over the western Kunlun Mountains, northwestern Tibetan Plateau, since the 1970s: Journal of Glaciology, v. 64, p. 624–636, https://doi.org/10.1017/jog.2018.53.

Yan, Q., Owen, L., Wang, H., and Zhang, Z., 2018, Climate constraints on glaciation over high-mountain Asia during the Last Glacial Maximum: Geophysical Research Letters, v. 45, p. 9024–9033, https://doi.org/10.1029/2018GL079168.

Yasuda, T., 2015, Glacier Surge Dynamics at the West Kunlun Shan Inferred from Satellite Remote Sensing [Ph.D. diss.]: Sapporo, Japan, Hokkaido University, 87 p.

Manuscript Accepted by the Society 23 December 2019
Manuscript Published Online 4 September 2020

Printed in the USA